EXPERIMENTAL STUDY OF CONFINEMENT EFFECT ON PHASE BEHAVIOR OF HYDROCARBONS IN NANO-SLIT CHANNELS USING NANOFLUIDIC DEVICES

A Dissertation

by

MEHRDAD ALFI

Submitted to the Office of Graduate and Professional Studies of
Texas A&M University
in partial fulfillment of the requirements for the degree of

DOCTOR OF PHILOSOPHY

Chair of Committee,	Hadi Nasrabadi
Co-chair of Committee,	Debjyoti Banerjee
Committee Members,	Stephen A. Holditch
	Eduardo Gildin
Head of Department,	Jeff Spath

May 2019

Major Subject: Petroleum Engineering

ABSTRACT

A great amount of hydrocarbon pore volume in unconventional petroleum reservoirs is distributed in pores of very small sizes, ranging from a nanometer to 100 nm pores. In such a small pore size, fluid–rock interactions play a dominant role in determining the phase behavior of hydrocarbons, which can lead to significant deviations in phase behavior, and significant errors in reserves estimation and reservoir simulations regularly performed by conventional simulators. In our research, we investigated the fluid flow and behavior of hydrocarbon liquids when confined in nano-sized pores. For this end, we employed state-of-the-art technology called lab-on-a-chip technology to mimic shale rock media in a nanofluidic chip. This novel method gives us the ability to directly visualize hydrocarbon liquid inside nano-sized pores and measure fluid properties. Using nanofluidic chips as a nano-scale PVT cell, we have been able to monitor the fluid phase behavior in nano-channels, and measure the bubble point temperature and its changes under confinement effect in pore sizes of 4 nm, 10 nm, 50 nm, and 100 nm. We have performed experiments for pure components of hexane, heptane, and octane, as well as binary mixtures of hydrocarbons (pentane/hexane, pentane/heptane) and a ternary mixture (pentane/hexane/heptane). We have also been able to measure the dynamic contact angle of hydrocarbons when confined in nanopores.

The results of our study show that at pore sizes of 10 nm and 4 nm, the confinement has a significate effect on alteration of hydrocarbon phase behavior by increasing the bubble point temperature. On the other hand, the quantity of such effects

on bubble point temperature is almost negligible at pore sizes of 50 nm and 100 nm. As reasoning for this phenomenon, at small pores confinement effect is significant in the form of molecule–pore interactions, which leads to a significant effect on bubble point temperature. However, the molecule–wall interactions that lead to alteration of the phase behavior of hydrocarbons do not have a significant influence on the phase behavior compared to the common molecule–molecule interactions at larger pores, leading to bubble point temperatures close to those of bulk media.

DEDICATION

In loving memory of my late beloved uncle and grandparents.

ACKNOWLEDGEMENTS

I want to express my gratitude to my advisor Dr. Hadi Nasrabadi, for his support throughout the course of this research. This work could not be done without his guidance and support. Also, I am grateful to my co-advisor Dr. Debjyoti Banerjee for his technical guidance and encouragement.

Furthermore, I would like to appreciate my committee members Dr. Stephen A. Holditch and Dr. Eduardo Gildin for their constructive comments.

Thanks also go to my friends and colleagues and the department faculty and staff for making my time at Texas A&M University a great experience.

Finally, I am so much grateful to my Mom and Dad for their infinite love and passion, to my lovely wife, Mehrangiz, for her unconditional support and patience, to my brother Masoud for his help, to my sweet little sister, Mahshid, and to my buddies, Vahid, Sara, and Nasser.

CONTRIBUTORS AND FUNDING SOURCES

Parts of this project was funded by the Crisman Institute for Petroleum Research and Berg-Hughes Center for Petroleum and Sedimentary Systems at Texas A&M University. Marathon Oil Company funded another part of this project.

This work was supported by a dissertation committee consisting of Dr. Hadi Nasrabadi (advisor) of the Department of Petroleum Engineering, Dr. Debjyoti Banerjee (co-advisor) of the Department of Mechanical Engineering, and Dr. Stephen A. Holditch and Dr. Eduardo Gildin of the Department of Petroleum Engineering.

NOMENCLATURE

σ	Surface tension (N/m)
ρ^L	Liquid density (kg/m^3)
ρ^V	Vapor density (kg/m^3)
$P_{\sigma i}$	Parachor factor
N_c	Number of components
MW_L	Liquid molecular weight (gr/mol)
MW_V	Vapor molecular weight (gr/mol)
Z_L	Liquid compressibility factor
P_L	Liquid Pressure (Pa)
R	Gas Constant (m^3 Pa K^{-1} mol^{-1})
T	Temperature (K)
Z_V	Vapor compressibility factor
P_V	Vapor Pressure (Pa)
Pc	Capillary pressure (Pa)
d	Channel depth (m)
w	Channel width (m)
θ	Contact angle (rad)
f_{iL}	Liquid fugacity (Pa)
f_{iV}	Vapor fugacity (Pa)
Φ_{iL}	Liquid fugacity coefficient

Φ_{iV}	Vapor fugacity coefficient
x_i	mole fraction of component *i* in liquid
y_i	mole fraction of component *i* in vapor
θ_{T1}	Contact angle at T_1
θ_{T2}	Contact angle at T_2
T_1	Temperature 1 (K)
T_2	Temperature 2 (K)

TABLE OF CONTENTS

LIST OF FIGURES

Page

LIST OF TABLES

1. INTRODUCTION*

1.1 Problem Statement

There is a big debate about the ways to mitigate the world's energy needs. Although the renewable sources of energy are on the rise, yet a big proportion of the world's energy is produced from petroleum resources. With the introduction of unconventional petroleum reserves and the viable techniques for the production of such resources, a great deal of research has focused on the investigation of such resources and their properties. Nowadays, unconventional resources have a dominant part in the world's energy play. Distributed majorly in 48 countries around the world with over 7576.6 trillion cubic feet and 418.9 billion barrels, shale gas and tight oil resources have proven to be a dependable source of energy for decades to come (Figure 1) [1]. It is worth mentioning that shale resources provided over 50 percent of U.S. oil production in 2016 [2].

---

* Parts of this chapter is reprinted with permission from "Experimental investigation of confinement effect on phase behavior of hexane, heptane and octane using lab-on-a-chip technology," M. Alfi, H. Nasrabadi, and D. Banerjee, *Fluid Phase Equilib.*, vol. 423, pp. 25–33, 2016. Copyright 2016 by Fluid Phase Equilibria, and "Effect of Confinement on the Dynamic Contact Angle of Hydrocarbons," M. Alfi, D. Banerjee, and H. Nasrabadi, *Energy & Fuels*, vol. 30, no. 11, pp. 8962–8967, Nov. 2016. Copyright 2016 by Energy and Fuels, and "Effect of Confinement on Bubble Point Temperature Shift of Hydrocarbon Mixtures: Experimental Investigation Using Nanofluidic Devices" M. Alfi, H. Nasrabadi, and D. Banerjee, *SPE Annual Technical Conference and Exhibition*. Society of Petroleum Engineers, San Antonio, Texas, USA, 2017 Copyright 2017 by SPE

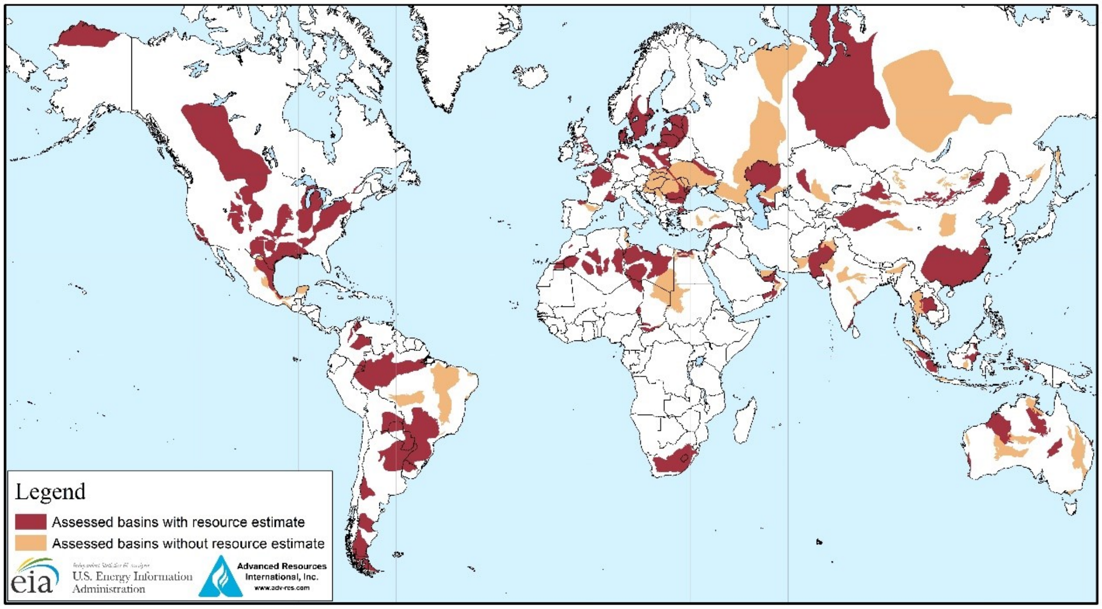

Figure 1- World's shale resources by country (Reprint with permission from [1]**).**

Although unconventional resources have proven to be a dependable source of energy, yet there are important challenges related specifically to such resources, which need to be addressed. The main challenge is the intrinsic differences between shale rock media and conventional reservoirs. The most notable difference arises from the fact that unconventional reservoirs, unlike conventional ones, comprise rocks with very small pore sizes. Figure 2 shows an SEM image of a typical shale sample from the Barnett Shale with porosity of 4.2% [3].

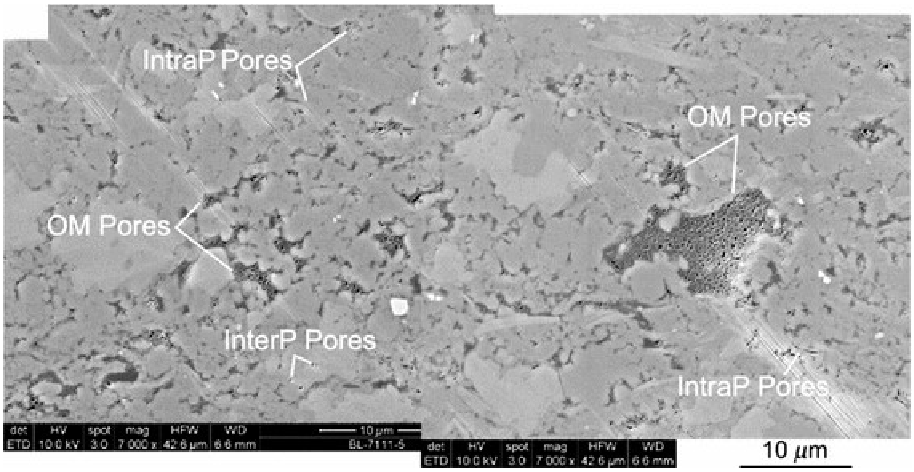

Figure 2- SEM image of a shale sample from Barnett shale formation (Reprint with permission from [3]**).**

Studies show that in a typical shale rock media, the majority of hydrocarbon-storing pores have sizes in the range of a nanometer to 50 nanometers [4], [5]. In such small pore sizes, due to the proximity of hydrocarbon molecules to the pore walls, molecule–wall interactions play a dominant role in the alteration of the thermodynamics and phase behavior of the confined fluid [6], [7]. Consequently, bulk thermodynamics fail to fully address the phase behavior of those fluids. This further extends to a direct effect on many calculations that are based on the phase behavior of hydrocarbon fluids, such as predicting well and reservoir productivity, reserves quantification, and estimating the success of enhanced-oil-recovery techniques [8]–[10].

1.2 Phase behavior

Phase behavior and thermodynamic properties are among the most important physical characteristics of a substance. Phase behavior is mainly referred to as the state in which a substance changes from one of the main phases to another, e.g. from solid to liquid, from liquid to gas, from solid to gas, or vice versa. Either of these changes happens due to a change in the intermolecular energies of the molecules forming the substance. Intermolecular bonds define the phase of a material. In solids, due to close packing of the molecules, these bonds are strong, and molecules are attached with a strong bond, while in gases the molecules are farther away and therefore the intermolecular bonds are weaker.

The phase behavior in systems containing a mixture of different components is more elaborated. Hydrocarbon systems and petroleum reservoirs mostly consist of a wide variety of components in a wide range of pressures and temperatures. As a result, such hydrocarbon systems can occur in various phases of gas, liquid, solid, or mixture of these phases. The complexities related to component mixtures coupled with porous media and reservoir rock physical properties lead to complex phase behavior of hydrocarbon reservoirs.

It is essential to have a comprehensive knowledge of the reservoir fluid once we want to perform a precise simulation or optimization on a field. A typical reservoir can have a pressure ranging from 300 psi to 3000 psi, and temperature ranging from 300 K to 400 K. There might be pressure variations at the production well or within the reservoir, all of which can highly affect the phase behavior of the reservoir. When referring to PVT properties, we are pointing at the volumetric behavior of reservoir fluid at different pressures and temperatures. For shale reservoir, unlike conventional reservoirs, there are additional complexities related to pore size and porosity, which play a dominant role in defining PVT properties in such reservoirs.

There have been several attempts to address the phase behavior of confined hydrocarbons using theoretical methods, such as Monte Carlo simulation [11]–[13], density functional theory [14], [15], and equation-of-state based models [16]–[20]. The ultimate goal of such models is to quantify the effect of confinement due to pore proximity on the overall phase behavior and critical property of reservoir fluids. For example, Neimark and Vishnyakov [11] performed molecular simulations using the gauge cell method based on the construction of a continuous adsorption isotherm in the form of a van der Waals loop. They were able to calculate energy barriers and equilibrium transitions between the metastable and stable states. They further compared the simulation results with experimental data from the capillary condensation of nitrogen on MCM-41 materials and ascertained the usefulness of the gauge cell method in the calculation of the overall phase envelope of confined systems. Pitakbunkate et al. [21] performed molecular dynamics simulation in order to drive phase diagrams for confined fluids. They used the Grand Canonical Monte Carlo simulation (GCMC) in which chemical potential, temperature, and pressure are kept constant, while the number of molecules changes. The focus of this work is mainly on density deviation as a result of small pore size. They conclude that confinement can cause a deviation of density compared to bulk as much as 69.8% for ethane, and 35.5% for methane. Li et al. [15] combined the engineering density functional theory with the Peng–Robinson equation of state to characterize the phase behavior and adsorption of substances in nanopores. They assumed that the Helmholtz free energy functional term consists of two terms: ideal-gas term and excess term. The former is a known term which accounts for the ideal part of the interactions. The latter term is further decomposed into two parts, the first part is extended from the Peng–Robinson equation of state and the second part is formulated by quadratic density expansion. They concluded that in a system of pure hydrocarbons, capillary condensation and hysteresis are more likely in heavier components. Kotdawala et al. [22] proposed a model based on density functional theory using an approximation of a narrow slit-pores. They focus on both polar and nonpolar mixtures and conclude that the effect of fluid–wall interactions are extensively higher than the fluid–fluid effect which draws the conclusion that the effect of pore size on phase behavior is much higher than the effect of pressure.

Travalloni et al. [18] chose the Peng–Robinson equation of state as the base equation for their work and implemented the effect of molecule–molecule and molecule–wall interactions by formulating an attractive part added to original Peng–Robinson equation. They tested the model for both pure component and a mixture of light hydrocarbons and measured the effect of confinement on the phase transition of such systems. Tan and Piri [19] used the perturbed-chain statistical associating fluid theory (PC-SAFT) coupled with the Young–Laplace equation in order to account for the curvature effect. Based on the equality of chemical potentials and adding the capillary pressure effect, they performed phase behavior modeling for pure hydrocarbons and binary mixtures. Derouane [20] used the van der Waals equation of state to describe the physical state of molecules adsorbed in microporous media, when the sites are fully saturated or near saturation conditions. They defined two terms for molecule–molecule and molecule–wall interactions. The result is somehow consistent with molecular dynamics simulation results, yet lacking experimental verification. Among the various modeling and simulation techniques available, the equation of state with capillary pressure modification has attracted the most interest for the simulation of shale reservoirs [23], [24]. This reveals the importance of investigating the validity of this technique.

Although these models provide us with a useful approach towards fluid phase behavior under confinement, reliable experimental data are needed to verify the validity of such calculations. There have been few attempts to address the confinement effects on PVT properties by using experimental tools [25], [26]. The majority of the experimental work in this area has focused on addressing the phase behavior by investigating the adsorption of liquids and gases in synthetic nanoporous materials such as MCM-41 [26], [27], activated carbon [28], [29], and Vycor and CPG [30]–[33]. For example, Qiao et al. [26] studied the effect of small pore sizes on the adsorption of hexane molecules at different temperatures. Based on what they have seen, the contribution of capillary condensation is dominant in adsorption isotherms. They used thermogravimetric analyses to investigate the adsorption isotherms of n-hexane on MCM-41 nonporous materials. By obtaining the adsorption isotherms of hexane adsorbed on different pore sizes of MCM-41 at different temperatures, they concluded that the effect of pore size on the hexane phase change is significant. Radhakrishnan et al. [28], on the other hand, investigated the phase behavior of CCl4 adsorbed in Vycor nanopores using experimental measurements and Monte Carlo simulation. They reported different condensation layers happening inside nanopores categorized as three different phases, which are depended on the pore width.

While the experiments performed on synthetic nanoporous materials implement indirect measurements of phase transitions inside the targeted system, a direct visualization method for investigating the phase behavior will provide us with a more robust tool for the verification of phase change at the nano-scale. Therefore, we used the novel technique of lab-on-a-chip technology to design a chip which features nano-sized channels etched on a glass substrate, in which the fluid movement and phase behavior can be observed by strong inverted microscopes [34], [35]. Devices built using this technology have a broad range of applications from biological sciences [36] to the oil industry. For example, Wang et al. [37] investigated the effect of confinement on the bubble point temperature of n-octane and hydrocarbon mixtures using this technique. They used a capillary pressure modified method to account for the effect of confinement. Their study was, however, limited to channels sizes of 100 nm deep, for which the confinement effect in terms of molecule–wall interactions is negligible. In another study, Zhong et al. [38] used lab-on-a-chip approach to investigate the capillary condensation of n-propane within 8 nm deep channels, and developed a model to predict the condensation propagation. However, to the best of our knowledge, there are currently no experimental measurements using this technique on the confined phase transition of other hydrocarbons in sub-10 nm channels, where confinement effect becomes significant.

1.3 Dynamic contact angle

Micro/Nanofluidic devices are used in various fields such as biomedical science, electrical engineering, fluid mechanics, and pharmaceutical science for both fundamental and applied research [39]–[43]. Such devices also provide methods to directly visualize fluid phase behavior. Such nanochannel devices are fabricated by standard semiconductor manufacturing processes [44]. Epi-fluorescence microscopy methods have been used to track the interface of gas/water flow in a 100 nm channel [45], where it is possible to obtain an image at a resolution as low as a single protein molecule [36].

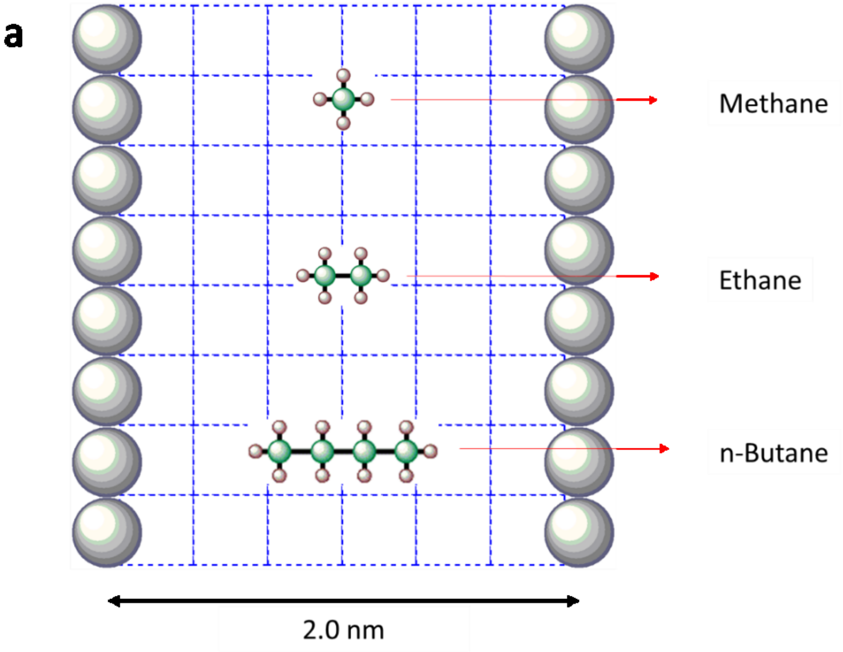

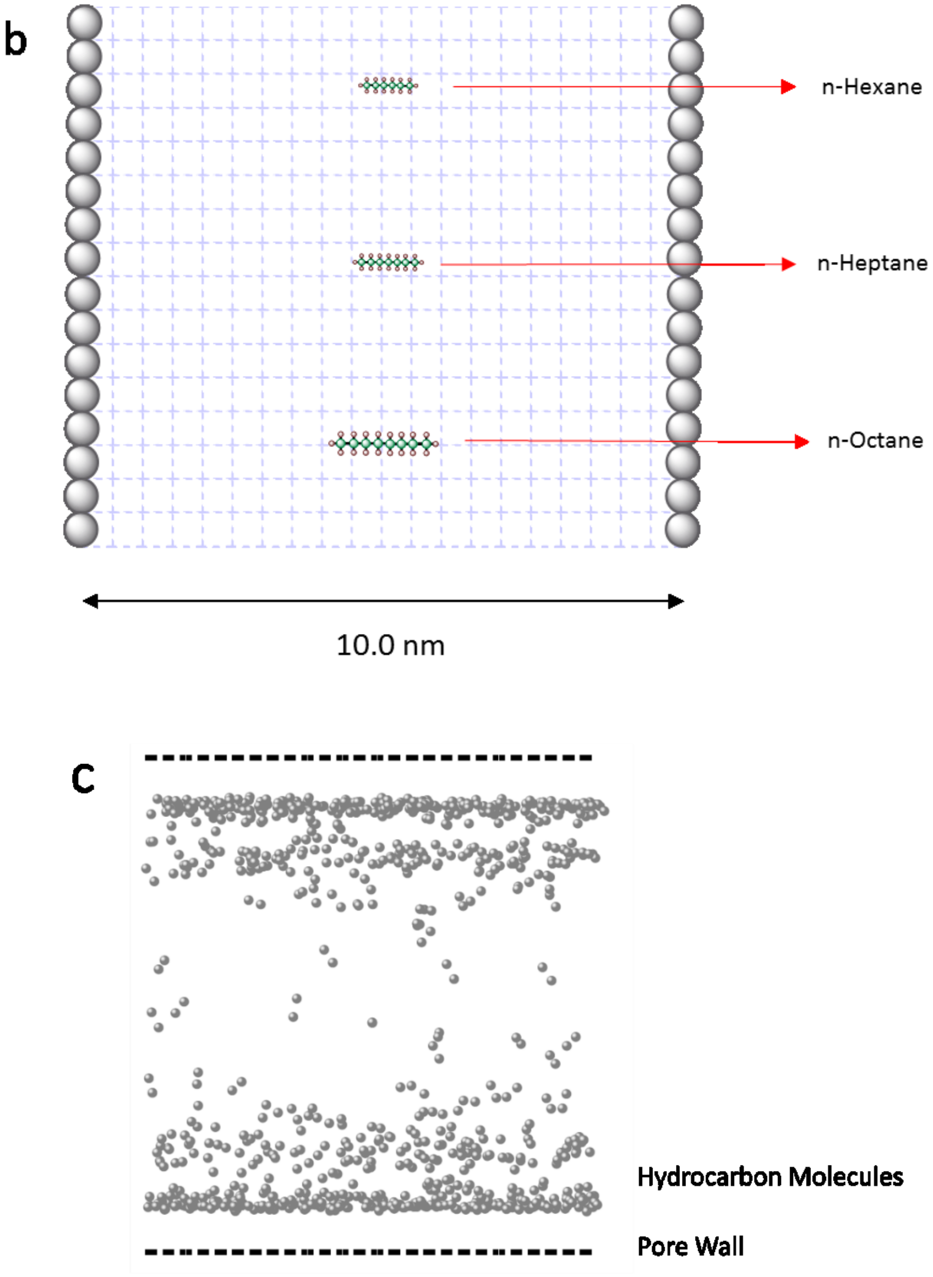

Figure 3- Scale comparison of hydrocarbon molecule size and shale rock pore size – a: the scale of light hydrocarbons when confined in 2 nm pore size; Methane (chain size 3.99 Å, lateral size: 3.99 Å), Ethane (chain size 4.76 Å, lateral size 4.41 Å), n-Butane (chain size: 8.24 Å, lateral size: 4.89 Å) b: Mid-size hydrocarbons confined in 10 nm channels (studied in this work). n-Hexane (chain size: 10.1 Å, lateral size: 5.21), n-Heptane (chain size: 11.24 Å, lateral size:5.39), n-Butane (chain size: 12.64 Å, lateral size: 5.73 Å) c: the actual alignment of molecules inside a nanopore based on molecular simulation (Reprint with permission from [35]**).**

Surface tension is an important force determining the shape of a liquid drop on a surface. In molecular terms, every molecule of liquid in bulk phase is pulled equally in all directions by other molecules in its immediate proximity, thereby resulting in a zero total force. However, when a drop of liquid is placed on a surface, molecules at the surface of the drop have fewer molecules in their proximity, and thus the force balance is changed. In such a case, the surface molecules are attracted by bulk molecules, leading to the creation of internal pressure, which is then further affected by the nature of stability that tends to cause the system to stabilize at the lowest surface free energy; the rounded shape of the drop satisfies this criterion.

The contact angle between liquid and gas phases is defined as the angle formed at the intersection of the liquid and the common surface of liquid/gas, in a gas-liquid-solid system (Figure 4). For a considerable time, wettability and contact angle measurements have been one of the most important topics in surface chemistry resear. Additionally, there has been a rising interest in wettability and contact angle measurements issues in the petroleum industry [46]–[48].

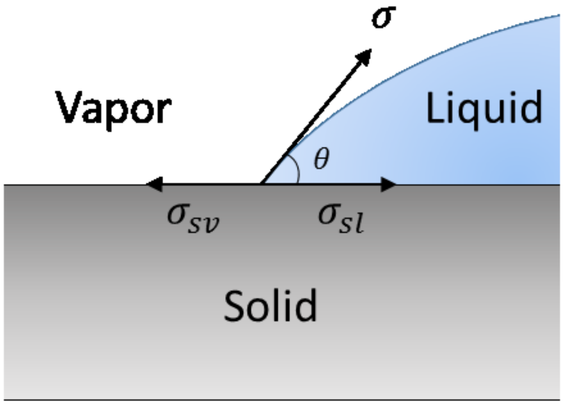

Figure 4- Diagram of the contact angle at the liquid-vapor interface (Reprint with permission from [35]**).**

In hydrocarbon reservoirs, it is very important to identify contact angles and wettability correctly, as these directly affect reserve estimates. There are several methods that can be used to measure the contact angle of gas-liquid systems. For example, techniques such as Direct Measurement using a Telescope-Goniometer [49]–[51], the Wilhelmy Balance Method [52], and the Capillary Penetration Method [53], [54] have been used extensively for making contact angle measurements. On the other hand, due to the strong surface-fluid interactions in nano-scale pores, the force balance cannot be predicted using the simplistic definitions previously-used by literature. Instead, it is necessary to consider complex interactions to theoretically calculate the contact angle [55]–[57]. In addition, there are complexities involved in experimentally measuring the contact angle at the micro and nano-scale droplets using direct visualization, and therefore it is common to measure the contact angle of a nano-sized liquid droplet by taking an AFM image of the sample. However, such methods need specific deposition techniques for placing nano-sized drops on the surface of a substrate for which the image is recorded [58], [59]. On the other hand, at such a small size the evaporation rate of the liquid is high which makes the droplet's surface moving and the AFM imaging process takes about 15 to 30 minutes, leading to inaccuracy of the image taken from the droplet's surface [60], [61].

The technique used in this study is a combination of lab-on-a-chip technology and high accuracy confocal microscopy. Hydrocarbon fluid is injected into micro/nano-sized channels where it becomes confined in nano-slits, and the gas/liquid contact angle is then measured using confocal microscopy. Previous research has studied thermodynamic property alteration due to confinement [62], but no experimental measurements have been conducted on the effect of confinement on the hydrocarbon dynamic contact angle. In this part of the research therefore, we used a nanofluidic device and high-resolution microscopy to measure the contact angle between pure hydrocarbons and the surface in nano-slit channels with depths of 10 nm. The significance of the proposed technique is to identify the effect of confined media on force balances and surface tensions that affect contact angle measurements.

1.4 Lab-on-a-chip technology for phase behavior

Lab-on-a-chip technology is a technique that integrates several laboratory functions in a single device. Devices built using this technology are mostly used in biomedical and biological sciences. Use of such devices can help scientists integrate several tests in a single device and therefore decrease the experimental time, substantially. In most cases, precise microscopy techniques are used to track the fluid path or to observe biological features. As a measure of precision, a single protein molecule can be observed under microscopes that are used in this technique [63]. The process of fabricating such devices is similar to the standard semiconductor manufacturing process [44]. One of the main features of such devices is that one can design, build, and use a unique chip based on common techniques. These devices can have sizes of below centimeter to a couple of centimeters and are mainly built out of silicon, glass, Polydimethylsiloxane (PDMS), or even paper.

Recent studies have revealed that microfluidic devices are reliable tools for measuring fluid phase behavior. However, there are a couple of challenges that get noticed when dealing with devices containing nano-sized channels. That is where microfluidic devices are separated from nanofluidic devices. In microfluidic devices, the channel depth can range from a few micrometers to hundreds of micrometers, while in nanofluidic devices the channel width is mostly kept on a few micrometer sizes while the depth can be as shallow as few nanometers.

The main advantage of investigating PVT properties using microfluidic devices is the time saved for performing a full PVT test [64], [65]. Mostowfi and Molla [64] performed PVT tests on a microfluidic device that contained a long serpentine microchannel etched on a silicon substrate, which is based on two-phase slug flow in microchannels. The pressure was measured inside the chip using membrane sensors, and the temperature was controlled using heaters. They designed nucleation restrictions in the channel to avoid supersaturation during the experiment and to make pressure drips along the channel (Figure 5-a). The result of their study shows a good match with conventional PVT cell experiments, which certifies the use of such techniques as accurate tools.

Xu et al. [65] designed a microfluidic device on a silicon platform that contains thousands of chambers. The channels have 15 micrometers depth and various widths. The working fluids get injected in and out of the chambers using inlet and outlet lines. A gas mixture saturates the channels first, and a working liquid is injected afterward to pressurize the gas trapped into the chambers. After this point, a pressure gradient is applied into inlet and outlet channels so that a distribution of pressure forms into the channels from one side to another. A temperature gradient is also imposed on the system perpendicular to the pressure gradient. The target here was to mimic the phase envelope by visualizing the fluid behavior inside the chambers (Figure 5-b).

a

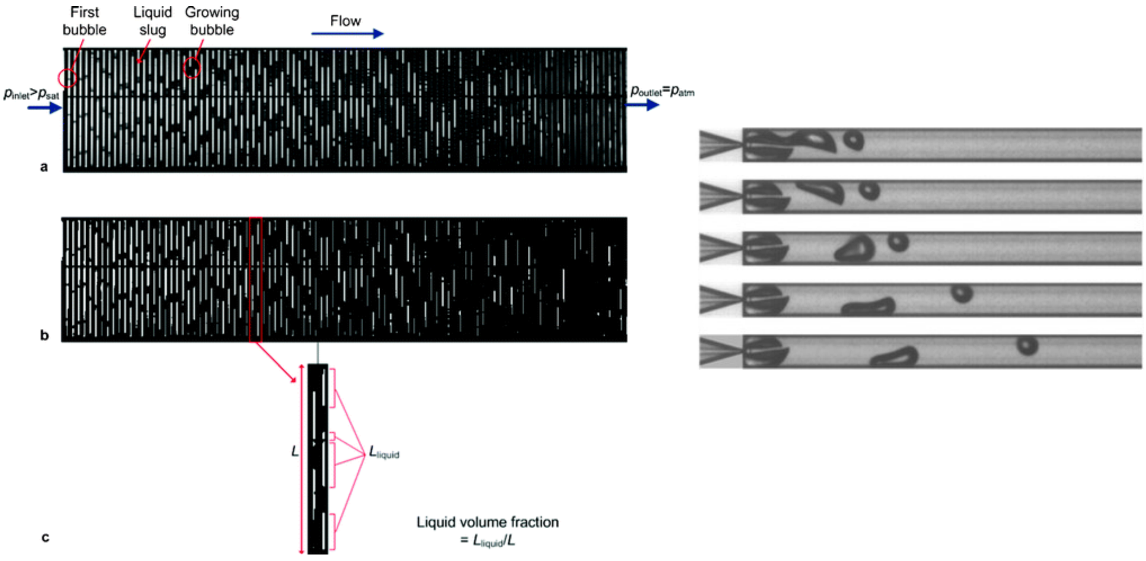

b

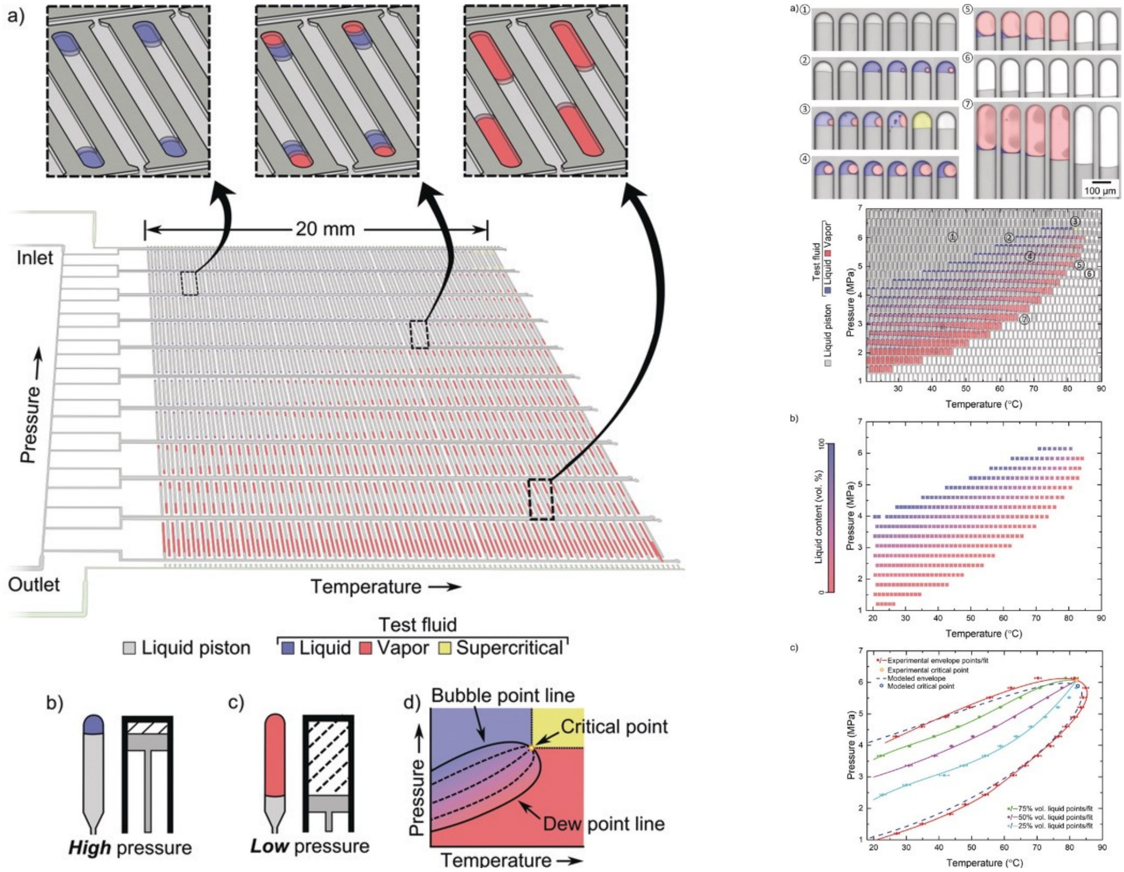

Figure 5- Microfluidic devices used for PVT test – a: single channel design with restrictions for pressure drop b: a full PVT scheme on a single chip (Reprint with permission from [64], [65]**).**

Microfluidic devices proved to be reliable when dealing with PVT properties of conventional reservoirs. In unconventional reservoirs, however, the story is totally different. In shale reservoirs, microchannels fail to mimic the rock media, owing to the fact that shale reservoirs consist of pores of nanometer size. Therefore, researchers have used nanofluidic devices, which feature nano-size depths for investigation of shale oil and gas phase behavior.

One of the first works done on the investigation of phase behavior in nanofluidic devices is by Wang et al. [37]. They used a device containing micro and nanochannels of size 10 µm by 10 µm, and 5 µm by 100 nm, respectively. They used microchannels to inject hydrocarbon into twenty nanochannels, which are target channels. Working fluids they used was pure n-pentane and a ternary mixture of n-butane, i-butane, and n-octane. Based on their observations, the fluid in microchannels evaporated before nanochannels, which they conclude that the confinement effect is the reason for this phenomenon. For pure hydrocarbons, this can clearly be the effect of confinement, although they did not record the onset of confinement affected bubble point temperature. For the case of hydrocarbon mixtures, however, after evaporation of the liquid in microchannels, the composition changes and lighter components tend to evaporate faster, making the residual liquid rich of heavy components and as a result, the delay in evaporation in nanochannels can no longer be accounted solely for confinement effect. This has been one of the most notable challenges in nanofluidic experiments and rarely been addressed.

In other studies, Zhong et al. [66], [67] studied phase behavior in nanochannels. In the first one, they investigated condensation of propane in 70 nm deep channels focusing both on continuous and discontinuous growth (Figure 6-a). They observed the effect of confinement on condensation where temperature and pressure are the variables and concluded that there is a notable difference when comparing the results to those of 100 nm channels. On the other work, they investigated the effect of confinement on dew point and bubble point pressure of fluid confined in 8 nm channels. They designed three sets of devices having micro and nano-sized channels with nano-size channels of depths

8 nm, 80 nm and 800 nm (Figure 6-b). They used microchannels to inject a mixture of methane and propane into nanochannels. The result of their study shows that at 8 nm channels, the dew point pressure is notably below dew point pressure of bulk phase and those of larger channels.

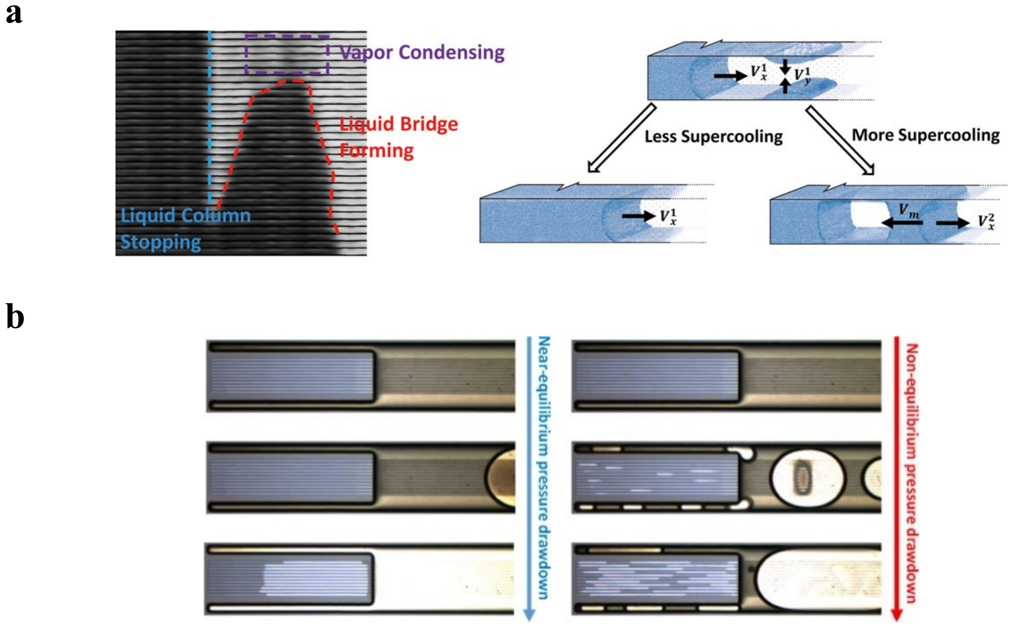

Figure 6- application of nanofluidic devices in phase behavior investigation under confinement - a: bubble point temperature of pure hydrocarbons and mixtures in 100 nm channels b: condensation of vapor in 70 nm channels c: dew point and bubble point pressure of hydrocarbon mixtures in 8 nm, 80 nm, and 800 nm channels (Reprint with permission from [66], [67]**).**

In our research, we designed and used silicon-based, and all-glass chips for investigation of fluid phase behavior. Figure 7 shows the real image of one of the chips we used for the investigation of fluid flow. This device was fabricated on a glass layer and bonded using another layer of glass.

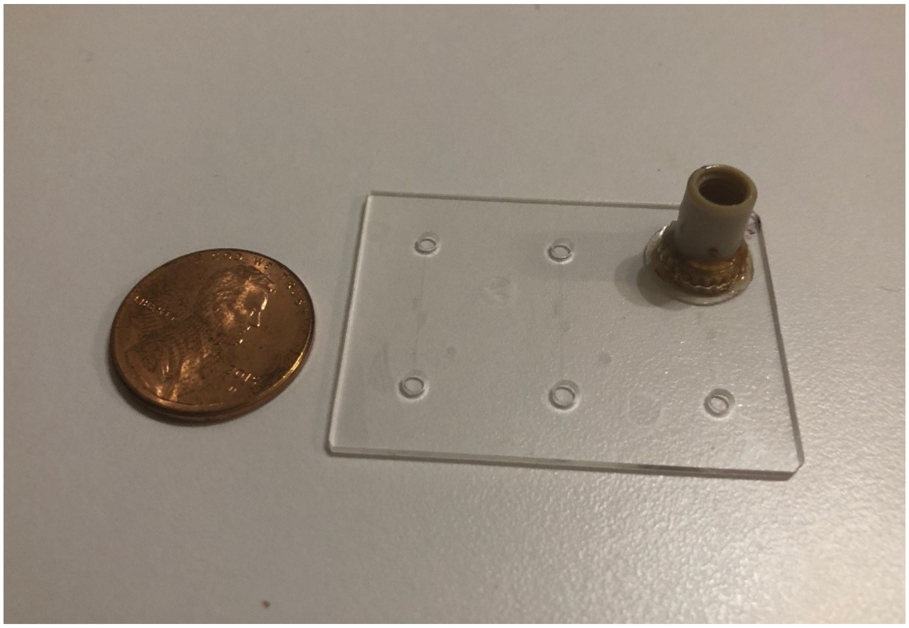

Figure 7- Image of the nanofluidic chip used in our experiments.

1.5 Included in This Dissertation

In this dissertation, we used state-of-the-art technology of lab-on-a-chip to investigate fluid flow and phase behavior of hydrocarbon liquids inside nano-sized channels. This includes the design, fabrication, and use of nanofluidic devices for investigation of hydrocarbon flow and phase behavior. To be more specific, the following studies are performed:

- Full process of fabricating nanofluidic devices using wet and dry etching. We tried various scenarios to achieve the best yield in fabrication of nanofluidic devices.
- Direct measurement of bubble point temperature and fluid flow for confined liquid hydrocarbons. For experiments conducted to measure bubble point temperature, we use microfluidic devices with channel sizes

of 100 nm, 50 nm, 10 nm, and 4 nm, while for fluid flow experiment, we use various sizes in a single chip.

- Comparison with a typical model which is used for calculation of bubble

1.6 Objectives

- Design and fabricate nanofluidic devices
- Test nanofluidic devices for investigation of fluid phase behavior under confinement
- Record bubble point temperature and fluid flow under confinement
- Compare the results with current models

2. METHODOLOGY[*]

In this chapter, I present the procedure for studying phase behavior by using a lab-on-a-chip approach. The rest of this chapter is organized as follows. I present the experimental methodology including the design and fabrication steps of our nanofluidic device, as well as the procedure for temperature control, visualization, and data acquisition.

2.1 Lab-on-a-chip technology

Lab-on-a-chip technology is employed to facilitate the integration of multiple laboratory functions in a small micro/nanofluidic chip. Devices fabricated by this technology are designed to handle fluid volumes metered to values as low as a few picoliters to femtoliters inside tiny narrow channels. The motivation behind the present work was to use lab-on-a-chip devices to mimic shale rock media and to be able to investigate the phase behavior inside nanometer-sized pores of shale rock. The device that was used in this work was a nanofluidic chip made of glass, which consisted of several parallel channels fabricated by photolithography.

---

[*] Parts of this chapter is reprinted with permission from "Experimental investigation of confinement effect on phase behavior of hexane, heptane and octane using lab-on-a-chip technology," M. Alfi, H. Nasrabadi, and D. Banerjee, *Fluid Phase Equilib.*, vol. 423, pp. 25–33, 2016. Copyright 2016 by Fluid Phase Equilibria, and "Effect of Confinement on the Dynamic Contact Angle of Hydrocarbons," M. Alfi, D. Banerjee, and H. Nasrabadi, *Energy & Fuels*, vol. 30, no. 11, pp. 8962–8967, Nov. 2016. Copyright 2016 by Energy and Fuels, and "Effect of Confinement on Bubble Point Temperature Shift of Hydrocarbon Mixtures: Experimental Investigation Using Nanofluidic Devices" M. Alfi, H. Nasrabadi, and D. Banerjee, *SPE Annual Technical Conference and Exhibition*. Society of Petroleum Engineers, San Antonio, Texas, USA, 2017 Copyright 2017 by SPE

2.2 Photolithography

Photolithography or optical lithography is the process of fabricating small chips by transferring a geometric pattern from a photomask to a photoresist material. This process consists of several steps (Figure 8). First, a photoresist is applied to the surface of the substrate, and then, a photomask is placed on top of these layers. The photomask, which is typically made of quartz or metal, is used to etch (develop) a specific pattern on the substrate, and the photoresist is then removed to complete the process. The entire surface is subsequently bounded by a layer of glass to form pores inside the chip.

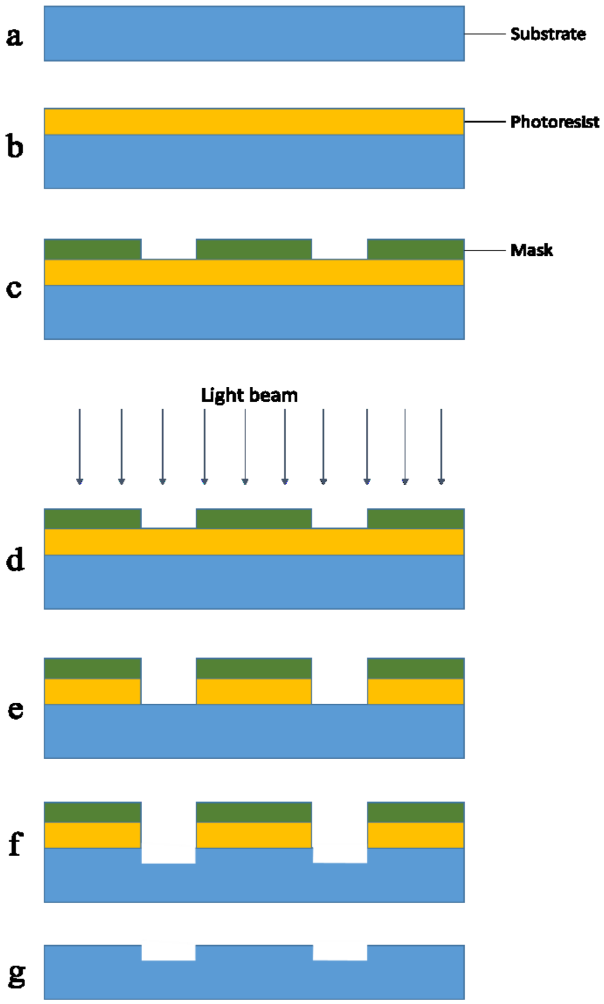

Figure 8- Photolithography process – a and b: a layer of photoresist is spin-coated on the substrate c: the photomask is mounted and aligned on top of the photoresist d: the pattern of the mask is replicated on the photoresist by illuminating the system e and f: the pattern is developed and etched on the substrate (using dry etching or wet etching techniques) g: the photoresist is removed (stripped). This process can be repeated, along with surface deposition of multiple layers of materials, for obtaining additional surface features until the desired pattern is obtained (Reprint with permission from [68]**).**

2.3 Nanofluidic chip

In this work, the lab-on-a-chip technology was employed to design a chip capable of mimicking shale rock media with acceptable accuracy. To this end, the proposed design consists of a glass substrate in which 20 parallel nanochannels connected to four reservoirs at the corners of the chip are etched using photolithography techniques combined with dry etching techniques (Figure 9). In order to reduce measurement error, we designed equally sized channels all over the chip. The nanochannels were capped by a glass substrate using a low-temperature glass bonding technique (the fabrication was performed by Klearia Company). Scanning electron microscopy (SEM) was used to image the nanochannels for confirming the desired feature sizes in the nanofluidic chip [69] (Figure 10).

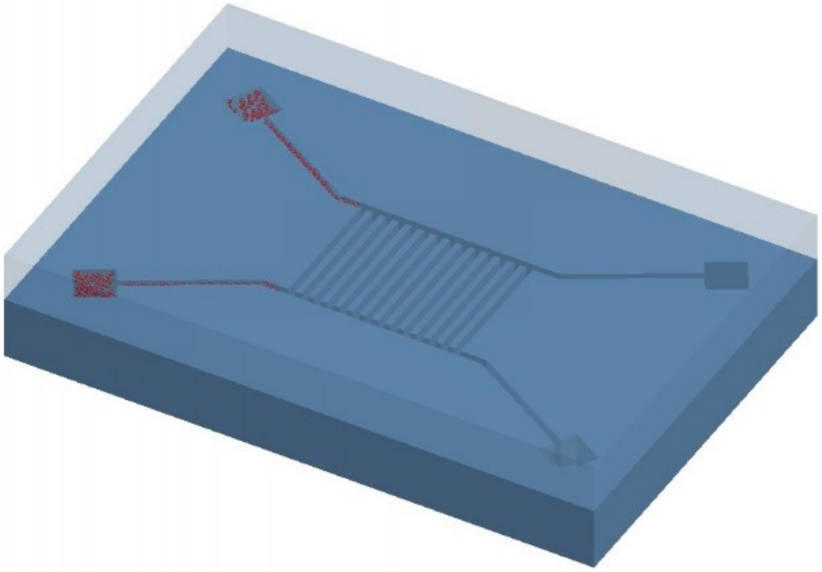

Figure 9- Schematic of the nanofluidic chip used in this work (with enlarged sizes).

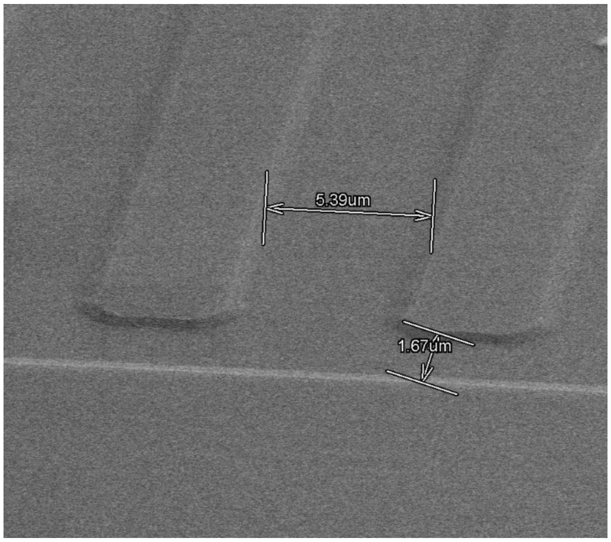

Figure 10- SEM image of the fabricated nanofluidic chip for calibration (Reprint with permission from [68]**).**

2.4 Temperature control

Temperature measurements were performed using three SA1XL thermocouples (purchased from OMEGA®). The thermocouples were attached to the chip's surface (both on the top and bottom surface in the vicinity of the visualization location of the nanochannels). An Infra-red (IR) camera was used to record the surface temperature of the chip. The IR camera was focused at the center of the chip where the nanochannels are located (Figure 11). In order to accurately measure the temperature at the center of the chip, all the thermocouples were thermally isolated using silicon glue. For calibration purposes, a heating plate was used as the heating source, and thermocouples were attached to its surface. In order to minimize the uncertainty arising from the temperature control system, we used highly controllable polyimide film heaters coupled with three thermocouples and LabVIEW as data acquisition. Thermocouples were attached to different locations of the system to accurately measure the temperature gradient. Calibration process has been performed for accurate measurements. The temperature was measured using two side thermocouples and a central thermocouple (Figure 12). As can be seen from Figure 12, the side thermocouples show a close temperature measurement owing to the uniform distribution of temperature on the chip. The procedure follows by increasing the temperature and observing liquid inside the channels. After performing calibrations, we conclude that a maximum of 0.5 degrees centigrade error is unavoidable due to fluctuations in room temperature.

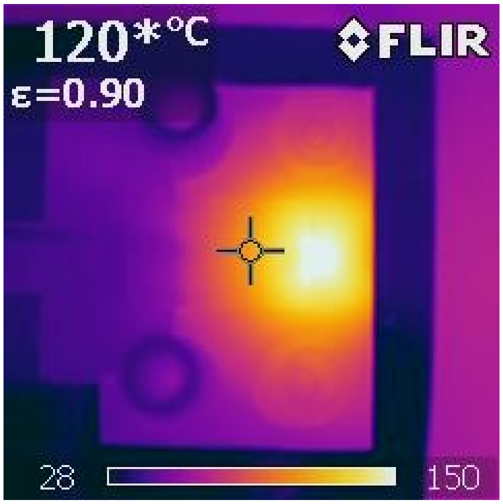

Figure 11- Image recorded by an IR camera is shown here. The measurements from the IR camera were validated using measurements from the surface mounted thermocouples for performing temperature calibration (Reprint with permission from [68]**).**

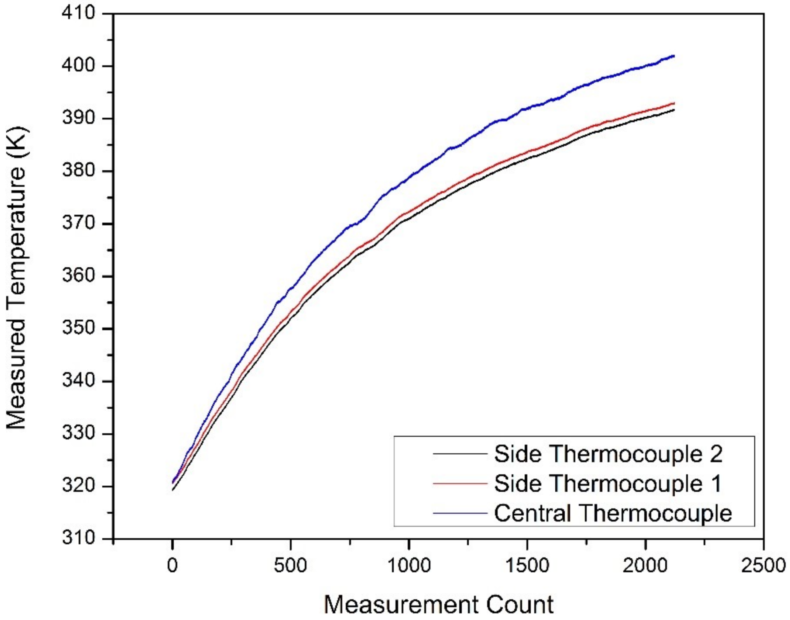

Figure 12- Temperature recorded at three thermocouples located at different sides of the chip. The main thermocouple is shown by the blue line, which is the central thermocouple. In order to capture the temperature gradient across the chip, two side thermocouples were attached to the chip in a symmetric manner (Reprint with permission from [34]**).**

2.5 Visualization and data acquisition

The nanofluidic chip contains four reservoirs that served as the source of the liquid for subsequent injection into the 20 parallel nanochannels, located at the center of the chip. The chip was packaged by bonding (using acrylic glue) Nanoports® (purchased from IDEX Corp.) on top of the four reservoirs. Each Nanoport was then connected to the injection system using PEEK tubing, valves, filters, and syringe pumps. The bubble formation phenomenon was visualized in real time and confirmed using an Olympus IX-81 inverted microscope (Olympus America, Center Valley PA, USA) equipped with a

UPLSAPO 20x/0.75 objective, a Rolera XR CCD camera (Qimaging, Surrey BC, Canada), and a Proscan H117 motorized XY stage (Prior Scientific, Rockland, MA, USA) controlled by the µManager freeware (http://www.micro-manager.org). A field lens with 1.6x magnification was used to achieve Nyquist sampling for imaging with the 20x objective. The following fluorescence filter sets (Chroma Technology Corp., Bellows Falls, VT, USA) were used, with the central wavelength and bandwidth of the excitation and emission filters as indicated: 543-nm HeNe laser and 560-nm long-pass filter.

The overall procedure of the experiment consists of mounting the nanofluidic chip under the microscope, injecting hydrocarbons into the channels by using a syringe pump, gradually heating the channels to the bubble point, and recording the bubble point temperature for each case (Figure 13).

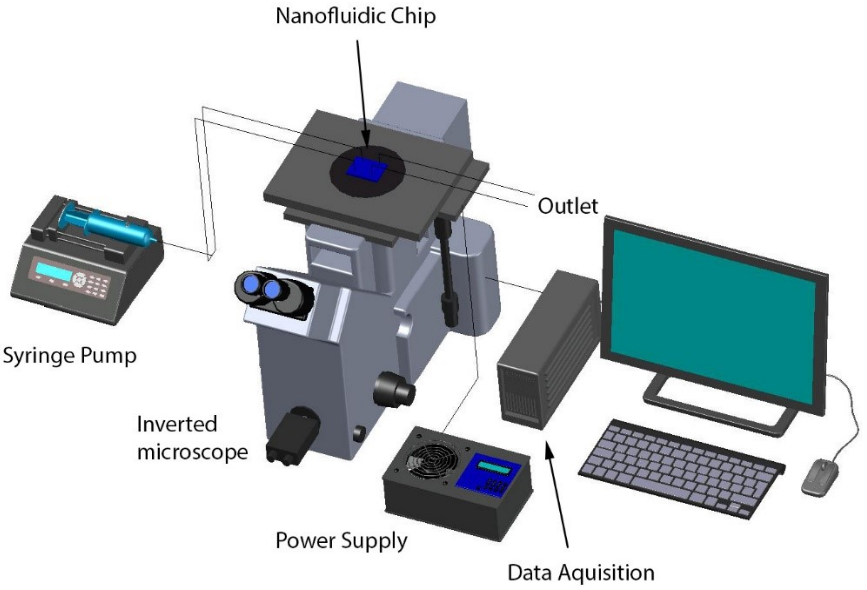

Figure 13- Schematic of the experimental apparatus. The syringe pump is connected to the chip using 0.02″ tubing. Inline filters are placed before the chip inlet to prevent any debris from entering the chip (Reprint with permission from [34]**).**

For the section of contact angle measurement, Pure hexane, heptane, and octane (Purity ≥0.99 by distillation, purchased from Sigma-Aldrich®) were injected into the reservoirs of the chip using a syringe pump. Before beginning the experiment, it was determined that no leakage or blockage had occurred in the reservoir-channel interface. The fluid inside the channels is in contact with both layers of glass, above and underneath the pore.

Due to co-existence of two phases inside the channels during evaporation, experiments were performed at two different temperatures for each hydrocarbon liquid, one at room temperature and the other at bubble point temperature, and the contact angle was measured in both cases. The liquid pumping rate at each section was constant achieving a constant pumping velocity of 3.1 μm/s.

3. RESULTS AND DISCUSSION[*]

In this chapter, I present the experimental and modeling results. I developed a numerical model for the phase behavior of a fluid confined in a nanochannel by combining the equation of state with the capillary pressure effect and performed experimental measurements to validate the predictions from the model.

3.1 Steps of fluid injection

A number of fluidic chips were designed and fabricated which contain twenty equally-sized arrays in a parallel set of micro/nanochannels with a single cross-sectional dimension (width 5 μm, various depth, and spacing 5 μm between nanochannels) [68], [70]. The array of parallel channels (tributary channels) is located at the center of the chip and is connected to feeding channels (artery channels) using the same size injection channels, and these are connected to four inlet/outlet ports representing storage reservoirs. Hydrocarbons of hexane, heptane, and octane with ≥99% purity (purchased from Sigma-Aldrich, Table 1) were injected into the channels, and the entire procedure was recorded using the camera connected to the microscope.

---

[*] Parts of this chapter is reprinted with permission from "Experimental investigation of confinement effect on phase behavior of hexane, heptane and octane using lab-on-a-chip technology," M. Alfi, H. Nasrabadi, and D. Banerjee, *Fluid Phase Equilib.*, vol. 423, pp. 25–33, 2016. Copyright 2016 by Fluid Phase Equilibria, and "Effect of Confinement on the Dynamic Contact Angle of Hydrocarbons," M. Alfi, D. Banerjee, and H. Nasrabadi, *Energy & Fuels*, vol. 30, no. 11, pp. 8962–8967, Nov. 2016. Copyright 2016 by Energy and Fuels, and "Effect of Confinement on Bubble Point Temperature Shift of Hydrocarbon Mixtures: Experimental Investigation Using Nanofluidic Devices" M. Alfi, H. Nasrabadi, and D. Banerjee, *SPE Annual Technical Conference and Exhibition*. Society of Petroleum Engineers, San Antonio, Texas, USA, 2017 Copyright 2017 by SPE

The experiments were divided into three steps. First, hydrocarbons were injected into the channels. This step should be performed extremely slowly owing to the high-pressure drop across the chip. The entire volume of the injected fluid was estimated to be approximately 10-5 µL. Second, the fluid inside the channels needs to stabilize in order for the pressure to reach atmospheric pressure. Third, after the fluid stabilizes inside the channels, electrical power is supplied to the heater, and the temperature is recorded simultaneously. We chose an initial temperature ramp rate of 12 °C/min for this process, which was subsequently reduced as the temperature of the chip approached the bubble point temperature.

Chemical Name	**Formula**	**Source**	**Mole Fraction Purity**	**Purification Method**
Octane	$CH_3(CH_2)_6CH_3$	Sigma-Aldrich	≥0.99	Distillation
Heptane	$CH_3(CH_2)_5CH_3$	Sigma-Aldrich	≥0.99	Distillation
Hexane	$CH_3(CH_2)_4CH_3$	Sigma-Aldrich	≥0.99	Distillation

Table 1- Specification of Chemical Sample.

3.2 Step one: Injection

In Figure 14a, the channels are fully saturated with pure hydrocarbon vapor. A suction syringe is used in this case to take the trapped air out and fill the channels with hydrocarbon vapor. The hydrocarbon liquid is injected from the top left and top right channels seen in Figure 14. As the fluid injection begins, the channels get partially filled with the hydrocarbon fluid (Figures 14b and 14c). We observed that the process of filling of nanochannels occurred in two different steps. In the first step, the entire set of nanochannels got partially filled with the injected liquid. However, for some of the nanochannels, the side-walls were not filled with liquid in this step (Figure 14d). As the injection proceeded, the unfilled parts of the channels began to be occupied by the hydrocarbon fluid (Figure 14e), until all parts of the channels were totally saturated with the liquid (Figure 14f). To sum up, Figure 14 shows a gradual movement of fluid into empty channels starting from Figure 14a proceeding to Figure 14f.

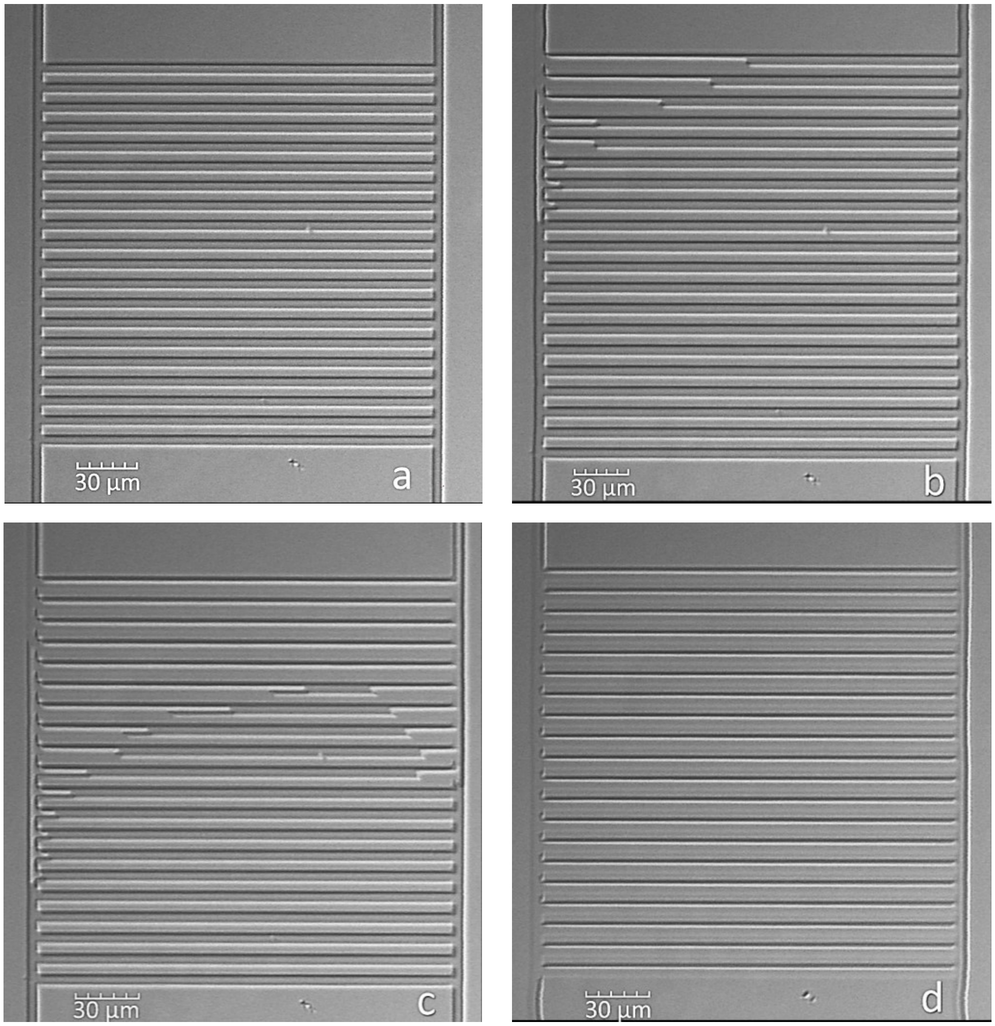

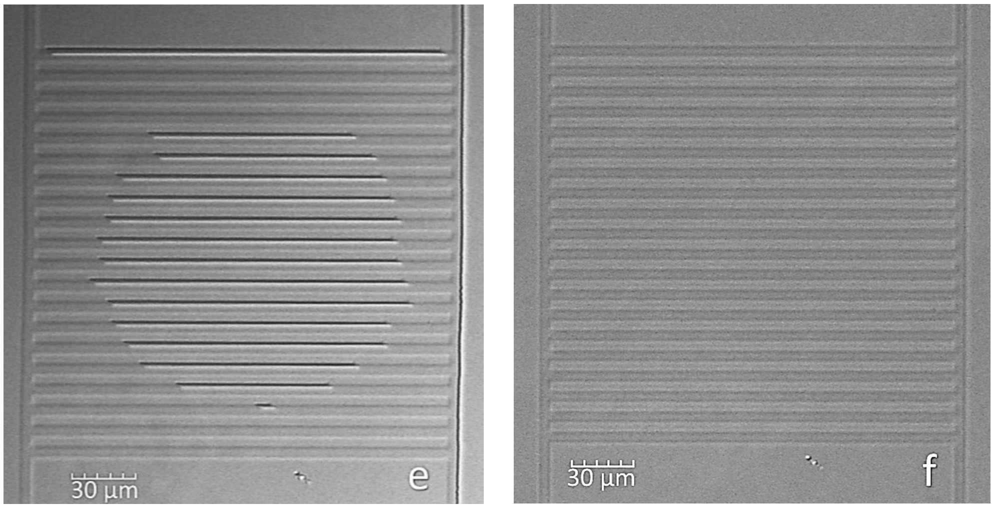

Figure 14- Step one: visualization of hydrocarbon injection into the nanochannel network – a: empty channels b: injection of hydrocarbons starts from the top-left channel c and d: as the fluid is pushed further into the channels, the empty bulk volume gets filled with the liquid e: with further pushing of the fluid, the parts of the channel wall that are dry get filled f: the process continues until the channels are fully saturated (Reprint with permission from [68]**).**

3.3 Step two: Stabilization

In this step, we needed to verify that the pressure inside all of the parallel nanochannels is equilibrated, which is expected to be the same as atmospheric pressure (since there is no flow). After the liquid fills the entire middle channels, injection is stopped, and fluid movement inside the channels is precisely observed. A good indicator of the pressure difference across the chip is the observation of fluid flow inside the channels. When there is no displacement of fluid inside the nanochannels across the whole chip, we can conclude that equal pressure is attained in the network of nanochannels. From a comparison of Figures 15a and 15b, we could easily see fluid movements inside the injection channels. In these figures, the liquid was observed to be moving inside the left-arm channel.

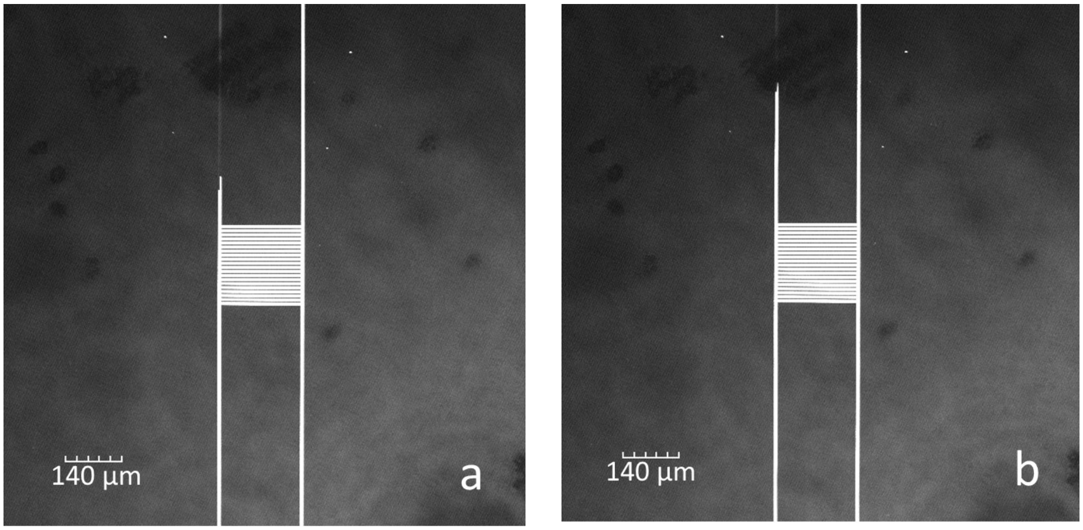

Figure 15- Step two: stabilization of fluid flow and pressure equilibration inside nanochannels. Before the temperature of the system is increased, pressure should be equilibrated over the entire network of nanochannels. The movement of hydrocarbon fluid inside longer channels was observed in order to confirm that there was no pressure difference along the chip. In these figures, comparing figures a and b, movement of fluid inside top left-hand side nanochannel is obvious (Reprint with permission from [68]**).**

3.4 Step three: Evaporation

After atmospheric equilibrium pressure was achieved throughout the chip, the heating procedure was started. A suitable temperature rise rate was achieved by gradually increasing the voltage from the power supply to the heater. By visually monitoring the nanochannels while the temperature was increasing, we were able to pinpoint the bubble formation. Bubble formation can be clearly seen in Figures 16a–16f. For bubble point determination, we considered the first bubble formed inside the channel as the reference for the bubble point temperature. It is noteworthy that bubbles start to form in a very short period of time as the temperature is increased; this can validate the homogeneity of the fluid-system employed in these experiments.

Starting from Figure 16a, the entire volume of the channels is occupied by the pure hydrocarbon liquid from the injection step. At this stage, a low contrast image can be seen due to existence of the liquid inside the channels. By heating up the chip at the center, the bubble point temperature is reached. As a result, the first signs of bubble formation appear inside the channels (Figure 16b). By further heating up the channels above the bubble point, bubble formation suddenly happens in the remaining channels in a few seconds (Figures 16c to 16e). The temperature at which the first bubble of vapor forms is recorded as the bubble point temperature. The process of heating continues until all of the liquid inside the channels get evaporated (Figure 16f).

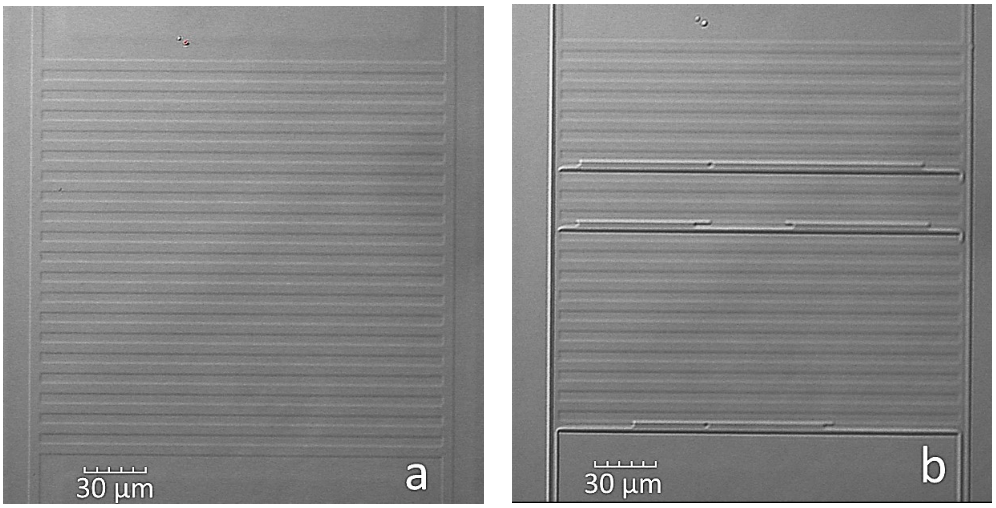

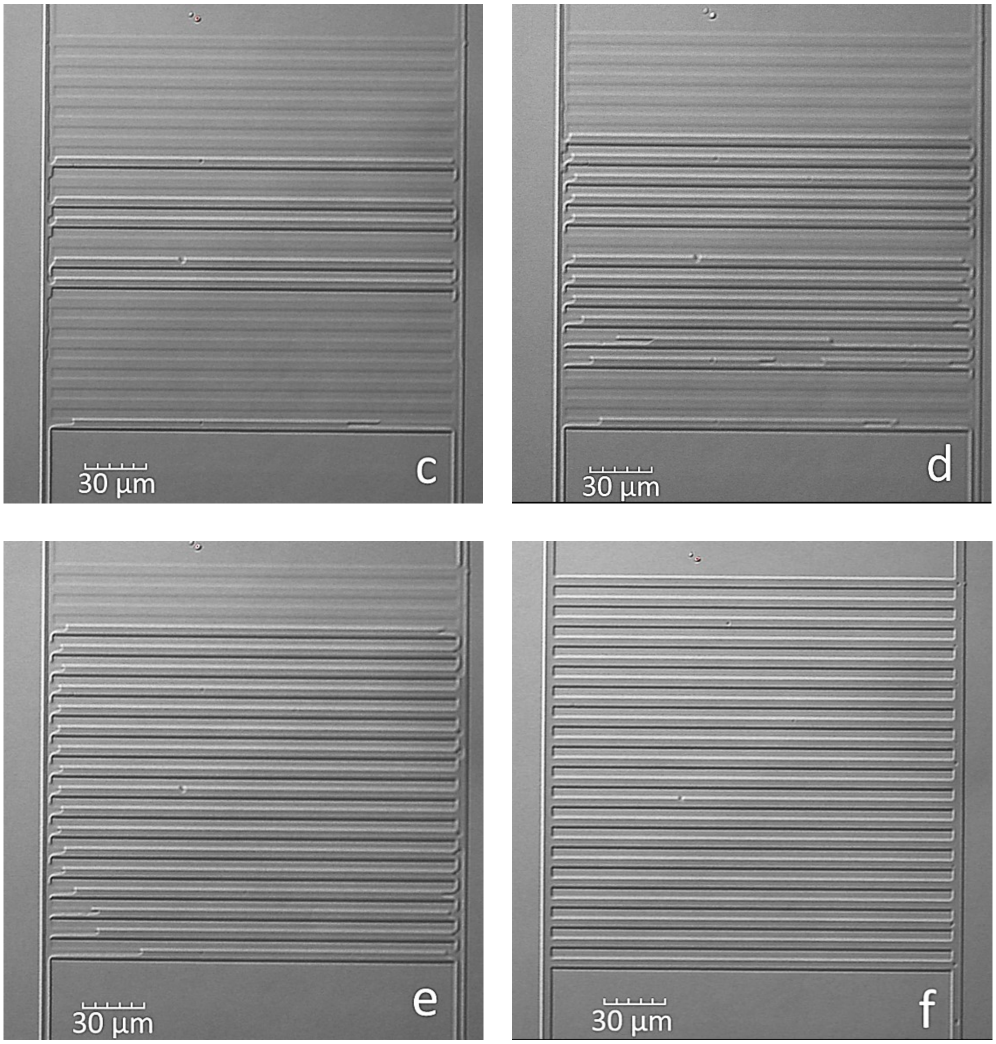

Figure 16- Step three: visual observation of bubble formation and evaporation of hydrocarbon fluid a: Nanochannels are fully saturated with hydrocarbon b: the first bubbles form inside the channels as the temperature is increased c–e: further increase in temperature leads to further bubble formation in multiple nanochannels f: The liquid inside the channels is fully evaporated (Reprint with permission from [68]**).**

3.5 Modeling of bubble point temperature for confined hydrocarbons

We used a modified version of the Peng–Robinson equation of state (PR-EOS) [71] to model the bubble point temperature for pure hexane, heptane, and octane. This technique has been extensively used for modeling of phase behavior [37], [72]–[75]. The technique entails calculation of the surface tension and the corresponding estimation of the capillary pressure. The capillary pressure is then used to correlate the vapor phase pressure, which is later substituted in fugacity calculations. Based on our preliminary design of 50-nm-deep nanochannels, modeling was performed for such channel sizes in this study. The surface tension in each case was calculated as follows [6], [76]–[78]:

$$\sigma^{1/4} = \sum_{i=1}^{Nc} P_{\sigma i}(\frac{\rho^L}{MW_L} x_i - \frac{\rho^V}{MW_V} y_i) \tag{1}$$

where

$$\frac{\rho^L}{MW_L} = \frac{P_L}{Z_L RT} \tag{2}$$

and

$$\frac{\rho^V}{MW_V} = \frac{P_V}{Z_V RT} \tag{3}$$

In these equations, $P_{\sigma i}$ is the parachor of component i; ρ^L and ρ^V are the liquid and vapor densities, respectively; and x_i and y_i are the molar fractions of component i in liquid and vapor, respectively.

Capillary pressure is calculated based on the Young–Laplace equation as follows [32], [79]–[82]:

$$P_c = 2\ \sigma\ cos\theta\ (\frac{1}{d} + \frac{1}{w}) \tag{4}$$

where θ is the contact angle, d is the nanochannel depth and w is the nanochannel width.

At the vapor-liquid equilibrium, the fugacity of a specific component in the liquid phase should be equal to that in the vapor phase:

$$f_{iL} = \Phi_{iL} x_i P_L \tag{5}$$

$$f_{iV} = \Phi_{iV} y_i P_V \tag{6}$$

Finally, the vapor phase pressure is correlated with the liquid phase pressure and capillary pressure as follows:

$$P_V = P_L + P_c \tag{7}$$

The properties used in these calculations were obtained from references [6], [78], [83]–[85].

The contact angle was directly measured in each case based on high-quality images. Image processing tools were used to highlight the interface between the gas and liquid phases.

Calculations were performed for models considering PR-EOS with capillary pressure modifications and without capillary pressure. The results are shown in Figure 17 and Table 2.

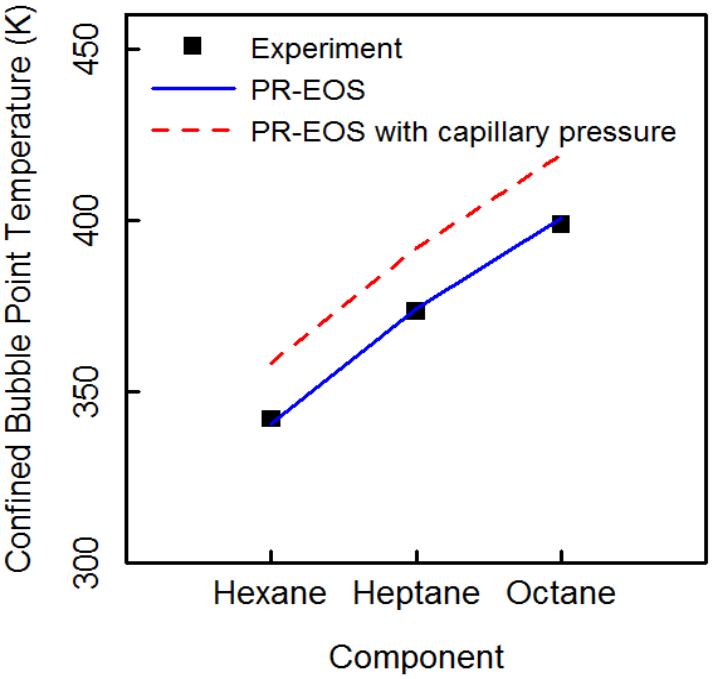

Figure 17- Comparison between the experimental measurements and results from PR-EOS model with the capillary pressure effect and PR-EOS model (without the capillary pressure effect) for Hexane, Heptane, and Octane. The error bar for experimental measurements is less than the symbol size (Reprint with permission from [68]**).**

Component	Capillary Pressure (Pa)	Bubble Point Temperature under Confinement (K)		
		Experiment	PR-EOS model without capillary pressure	PR-EOS model with capillary pressure
Hexane	368016.24	341.9±0.4	340.7	358.1
Heptane	368635.15	373.3±0.2	374.4	391.8
Octane	368927.93	398.7±0.3	400.7	419.2

Table 2- Confined bubble point temperatures measured and modeled for three hydrocarbons. Each measurement was repeated three times to assure the accuracy of the results (Reprint with permission from [68]**).**

The resulting bubble point temperature calculated using this model for a 50-nm-deep channel containing hexane, heptane, and octane as the hydrocarbon fluid is compared with experimental results obtained from microfluidic chips with the same size. Experiments were repeated three times to ensure the validity of the data obtained and minimize human error. As the molecular size increases from hexane to octane, we expect to see higher bubble point temperatures since the molecular bounds become stronger in larger molecules. It can be drawn from the results obtained that the bubble point temperature measured at 50 nm channel is very close to calculations based on the PR-EOS without accounting for capillary pressure. Therefore, it can be concluded that at pore sizes as small as 50 nm, the commonly used PR with the capillary pressure model is not accurate enough.

In the capillary pressure calculations, the surface tension of the confined hydrocarbons is estimated by neglecting the curvature effect. Furthermore, the parachor factors are based on a simplistic model that can be applied only to larger-sized channels.

3.6 Effect of Pore Size on Pure Hydrocarbon Phase Behavior

Pure hydrocarbon liquids of n-hexane, n-heptane, and n-octane were injected into channels of 100 nm, 50 nm, 10 nm and 4 nm depth and the entire procedure was recorded using the camera attached to the microscope.

Table 3 summarizes the results of our experimental measurements. The measured values for the bubble point temperature of 100 nm channels are very close to those of a non-confined bulk hydrocarbon for all three cases of n-hexane, n-heptane, and n-octane. There is a good agreement between the bulk bubble point temperature and our measurement of bubble point temperature in 100 nm channels, which proves the accuracy of the measured bubble point temperature using our temperature control system. For smaller-sized channels of 50 nm depth, the recorded bubble point exhibited a slight shift compared to those of the 100 nm channels and the bulk media, but the magnitude of this shift was not significant pointing to negligible confinement effect in the 50 nm channel sizes. However, at smaller-sized channels of 10 nm depth, there was a notable change in the bubble point of all three hydrocarbons. At this size, the measured bubble point temperature shows a significant shift (increase) compared to those of the 100 nm and 50 nm channels. We can conclude from these observations that, at 10 nm channel size, the effect of confinement due to the molecule–wall interactions becomes significant and plays a notable role in the alteration of liquid phase behavior. More interestingly, as we take a step further and perform experiments on 4 nm channels, the effect of confinement is even more pronounced. We noticed even a larger increase in the bubble point temperature in the 4 nm channels, in which the hydrocarbon molecules are only a few times smaller than the pore size. These results clearly show the effect of confinement on liquid phase behavior.

Hydrocarbon Liquid	**Bulk Bubble Point Temperature (K)**	**Experimental Measurement-Bubble Point Temperature (K)**			
		100 nm pores	**50 nm pores**	**10 nm pores**	**4 nm pores**
n-hexane	340.4	340.5±0.5	341.1±0.4	350.8±0.4	354.1±0.3
n-heptane	372.3	373.3±0.4	373.8±0.2	382.5±0.5	386.0±0.5
n-octane	399.1	398.7±0.7	399.2±0.3	409.1±0.6	413.4±0.5

Table 3- Bubble point temperatures for different hydrocarbon cases compared to bulk bubble point temperatures. Pores with 10 nm size and below show an obvious shift in the bubble point temperature compared to bulk media.

Figure 18 shows the shift in the bubble point temperature of pure hydrocarbons compared with the bulk bubble point temperature.

a

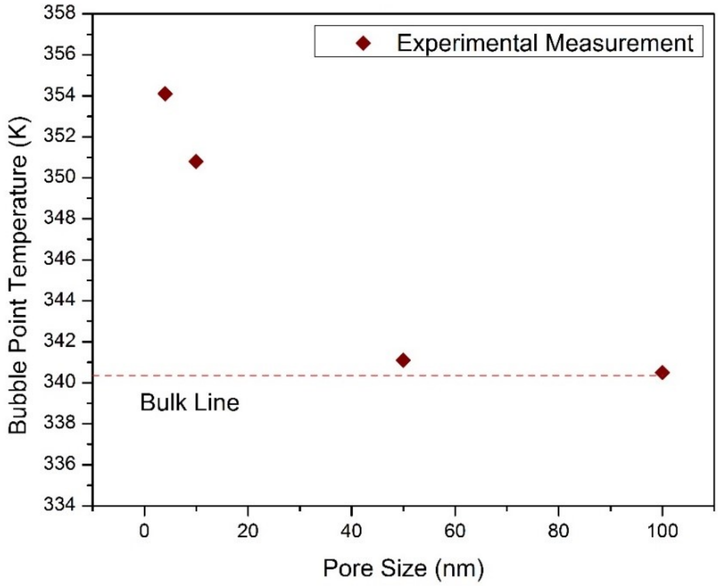

b

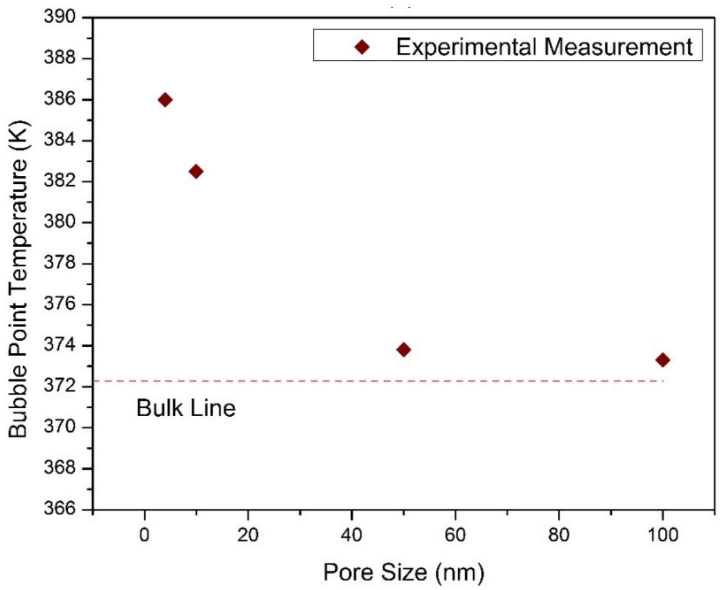

c

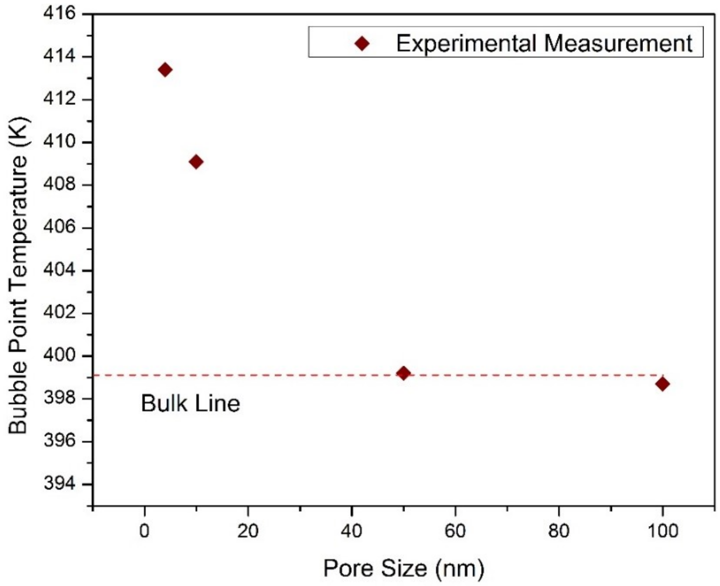

Figure 18- Experimental measurements compared to bulk bubble point temperature - a) n-hexane b) n-heptane c) n-octane. For channel sizes of 10 nm and 4 nm, we saw an obvious shift in bubble point temperature compared to the bulk bubble point.

It can be inferred from Figure 18 that bubble point temperature of pure hydrocarbons confined into nano-sized channels does not show a shift compared to bulk media at channel sizes of 50 nm and larger. However, as the channel size decreases, the molecular size of liquid hydrocarbon becomes comparable to the channel size, which means higher interaction with the channel wall. As a result, the phase behavior of confined liquid hydrocarbon shows significant changes. These changes become more pronounced as we move further into smaller size channels.

3.7 Hydrocarbon Mixtures

We also performed experiments on binary and ternary hydrocarbon mixtures injected into channels of 100 nm, 50 nm, and 10 nm. The results of the experimental measurements are presented in Figure 19. The bubble point temperature recorded for 100 nm deep channels is close to those of the bulk bubble point temperature, for three cases of hydrocarbon mixtures, as expected from literature review [6], [78]. The small difference between the bubble point temperature measured at 100 nm channels and the flash calculation bulk bubble point temperature validates creditability of our technique and accuracy of our method for measurement of bubble point. At 50 nm channels, the typical capillary pressure-based equation of state calculations predict a shift in bubble point temperature [68]. However, we have seen almost no shift in the bubble point temperature compared to the bulk situation. In this case, the amount of difference is not significant to be accounted as the effect of confinement on the bubble point temperature. However, as we move forward to the chip with 10 nm channels, the bubble point temperature shows a different behavior. The liquid confined in 10 nm channels shows a bubble point temperature higher than bulk bubble point temperature at all three cases of hydrocarbon mixtures. This can be interpreted as when the pore size decreases to 10 nm, the effect confinement leads to alteration of phase behavior in bubble point temperature, as a result of the pore proximity, in which molecule–wall interactions have considerable values. This clearly certifies the role of the intensity of the molecule–wall interactions on hydrocarbon phase behavior. This size, however, is very close to the limit of our measurements, since the injection of liquid molecules inside smaller size pores is extremely difficult, and also the layer of liquid placed in the pores smaller than around 4 nm would not make enough contrast for the microscope to precisely visualize the phase transition without use of fluorescent dyes. We avoided using fluorescent dyes in this study, because they perturb the purity of the liquid, leading to the inaccurate measurement of bubble point.

a

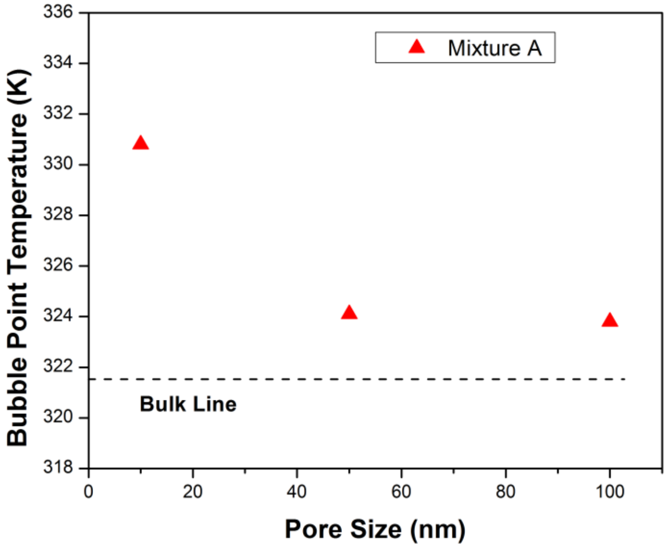
Mixture A
Bubble Point Temperature (K)
336
334
332
330
328
326
324
322
320
318
Bulk Line
0
20
40
60
80
100
Pore Size (nm)

b

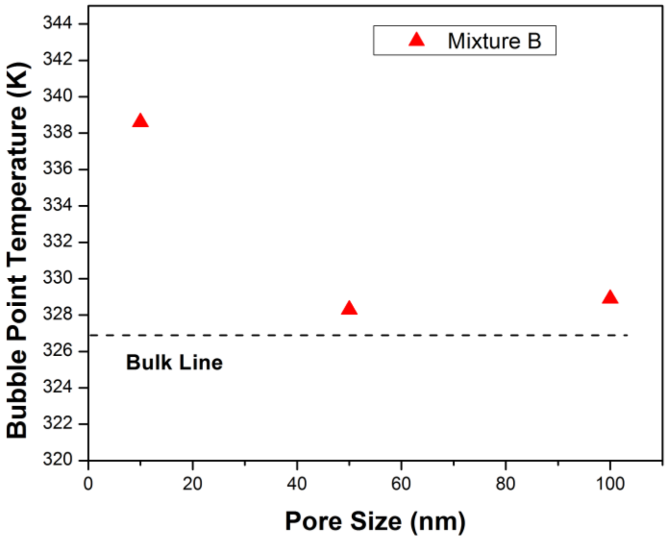
Mixture B
Bubble Point Temperature (K)
344
342
340
338
336
334
332
330
328
326
324
322
320
Bulk Line
0
20
40
60
80
100
Pore Size (nm)

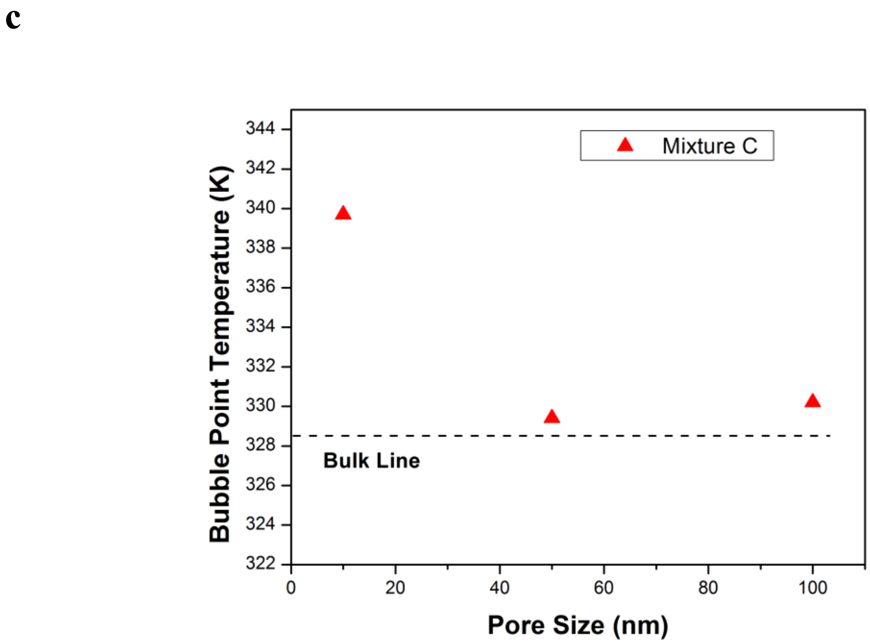

Figure 19- Experimental measurement of the bubble point temperature of three hydrocarbon mixtures in different pore sizes. Mixture A has 50% Pentane and 50% Hexane, Mixture B has 50% Pentane and 50% Heptane, and Mixture C has 40% Pentane, 30% Hexane, and 30% Heptane (Reprint with permission from [34]**).**

Hydrocarbon Liquid	Bulk Bubble Point Temperature (K)	100 nm pores	50 nm pores	10 nm pores
50% Pentane - 50% Hexane	321.57	323.8	324.1	330.8
50% Pentane - 50% Heptane	327.24	328.9	328.3	338.6
40% Pentane - 30% Hexane - 30% Heptane	328.43	330.2	329.4	339.7

Table 4- Recorder bubble point temperatures for different cases of hydrocarbon mixtures (Reprint with permission from [34]**).**

3.8 Dynamic contact angle

The contact angle between the liquid hydrocarbon and the glass wall was measured precisely using ImageJ software, where images from the liquid-air interface were selected at different locations inside the channels and then measured using the angle measurement tool. Figure 20 shows microscopic images taken from the nanochannels when partially filled with a pure hydrocarbon, and the contact angle was then measured using the sample shown in Figure 20 (middle image). The schematic shown in Figure 20 presents the logic for measuring the dynamic contact angle inside the nanochannels.

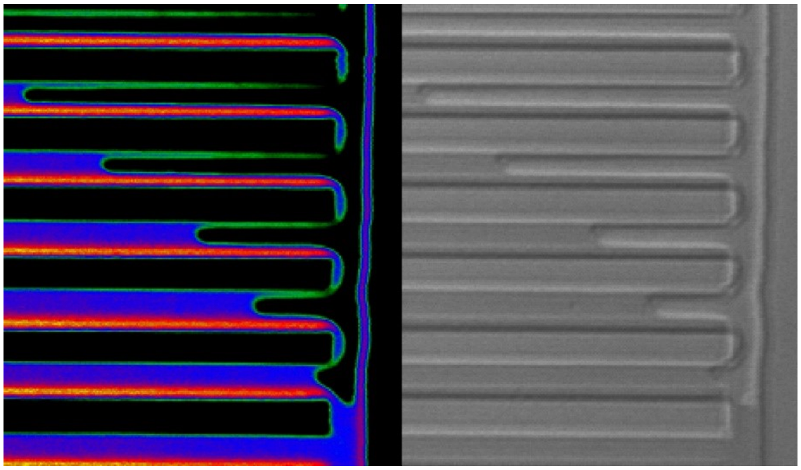

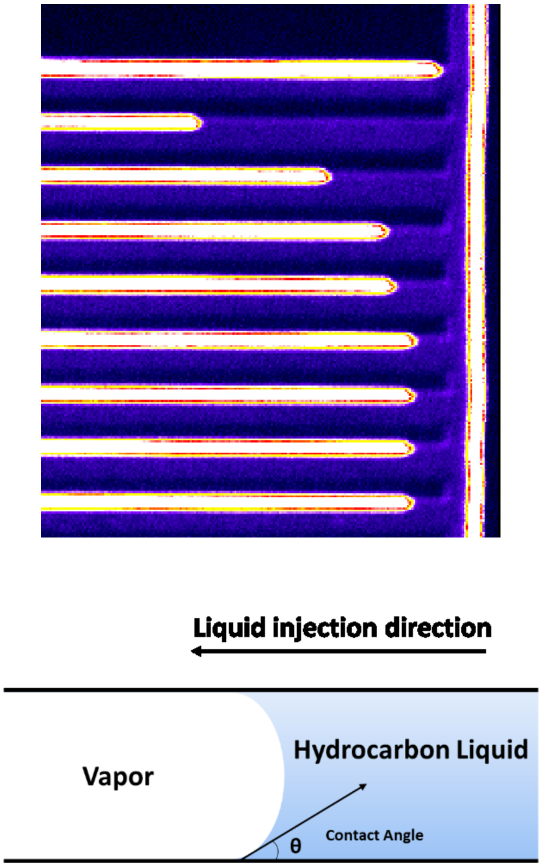

Figure 20- Microscopy images taken from the sample hydrocarbon (top and middle). Schematic of the channels while the liquid is pumped into the nano-sized channels (bottom) (Reprint with permission from [35]**).**

As previously mentioned, measurements of the contact angle between the liquid and the solid surface were conducted at two different temperatures. The measurements were found to be consistent, even though a ±1 degree error was found to exist for some of the channels measured due to the quality limit of the images taken.

Experimental measurements of the contact angle in confinement were compared to those of conventional measurements. We measured the gas-liquid contact angle at two different points on the chip; the first measurement refers to the contact angle measured at the bulk phase, where no nano-sized channel existed and where the fluid was freely in contact with the solid and the gas. The second measurement was taken where the liquid was confined within the 10-nm deep channels. Based on a comparison of these measurements, an obvious shift in the contact angle could be determined when the fluids were confined inside the nano-slit pores. Figure 20 shows this shift for the three hydrocarbons. It can be concluded that the confinement contributes significantly to a change in the contact angle, which can be further extended to change in the wettability of porous media due to confinement. This will be a very important observation since it will significantly affect production from unconventional reservoirs.

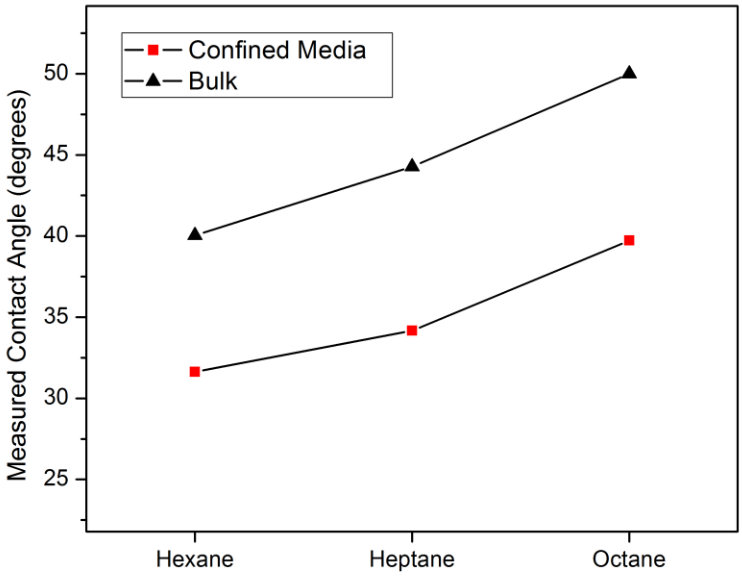

Figure 21- Comparison of contact angle measured for confined media and bulk media (T = 26.1℃). (The error bar is smaller than the size of the symbols) (Reprint with permission from [35]**).**

We then investigated the dependency of the contact angle on temperature when confined inside the nano-sized channels. Based on previous correlations, the temperature dependency of the contact angle in the system we used, which consisted of liquid hydrocarbon injected into silica chips, could be predicted by the equation 8 [86]–[89]:

$$\theta_{T2} = \theta_{T1} + 0.1 \times (T_1 - T_2) \qquad (8)$$

where θ_{T1} and θ_{T2} are contact angles at temperatures T_1 and T_2, respectively.

Table 5 shows a comparison between the contact angles measured at room and bubble point temperatures for pure hexane, heptane, and octane, respectively, and those using conventional methods.

Hydrocarbon	**Temperature (K)**	**Measured Hydrocarbon Contact Angle (Degrees)**	
		Bulk	**Confined**
Hexane	296.2	40.1±0.5	31.6±0.5
	340.7	35.6±0.4	28.1±0.4
Heptane	296.2	44.3±0.5	34.2±0.5
	374.4	36.4±0.5	27.4±0.5
Octane	296.2	50.0±0.4	39.7±0.4
	400.7	39.6±0.5	31.1±0.5

Table 5- Measurements of contact angles for hydrocarbons at room and bubble point temperatures with and without confinement effect (Reprint with permission from [35]**).**

Measurements of contact angles for the three cases of pure hydrocarbons were performed at two temperatures, room temperature, and bubble point temperature. The contact angle measured in the nano-sized channels decreased with an increase in temperature for all hydrocarbons. This shows that although the contact angles measured in the confined pores shifted significantly compared to results using conventional bulk measurements, the trend of contact angle change with temperature was almost the same as that for bulk properties.

4. CONCLUSIONS AND FUTURE REMARKS

Nanofluidic chips with channels of 100 nm, 50 nm, 10 nm, and 4 nm depth, and 5-μm width were fabricated for this research. The goal of this work was to investigate the confinement effect on the bubble point temperature of hydrocarbons using a novel method of lab-on-a-chip. The high-tech nanofluidic devices were fabricated, tested and employed for investigation of the phase behavior of hydrocarbons. Pure hydrocarbons of hexane, heptane, and octane, and binary and ternary mixtures of hydrocarbon liquids were used as the hydrocarbon fluid, and the bubble point temperature was measured using nanofluidic devices. At the bubble point temperature, because of the phase contrast between liquid and gas phases, we were able to spot the bubble formation inside the channels and measure the bubble point temperature for those liquids confined inside the channels. A model based on the Peng–Robinson equation of state, which has mostly been used in reservoir simulations, was applied as a typical model. It can be concluded from these measurements that at a channel sizes of 100 nm and 50 nm, the confinement effect on the bubble point temperature is almost negligible, which is in good agreement with the results reported in [78]. However, the confinement effect has a significant role in shifting the bubble point temperature of liquids confined in channels of 10 nm and 4 nm in size. Additionally, a comparison of the experimental results with those of the model reveals that at pore sizes as small as 50 nm, the capillary-pressure-based models fail to describe the phase behavior of hydrocarbons inside confined media and such models cannot be used for accurate reservoir simulations.

Furthermore, nanofluidic chips were used to visualize the contact angle using optical and confocal microscopy techniques. Preliminary experiments were performed using a fluidic chip with channels of 10 nm depth, and flow visualization of the nanochannel filling was conducted using optical and confocal microscopy techniques for the three case of pure hydrocarbon, hexane, heptane, and octane.

Values for different contact angles and dependency on temperature reported in the literature were compared with those obtained using our nanofluidic device. Results from bulk measurements indicated that a significant deviation in the contact angle could occur for fluids confined in pore sizes of 10 nm. The temperature dependency of the contact angle was then investigated using measurements performed at room temperature and the hydrocarbon bubble point. Results showed the trend of contact angle change with temperature to be consistent, both with pore confinement and without confinement.

We concluded from these observations that the confinement effect due to the molecule–wall interactions starts to play a dominating role in the alteration of the hydrocarbon phase behavior and the dynamic contact angle at pore sizes of 10 nm and below.

In the future, we will develop a setup for investigation of fluid phase behavior in nanofluidic devices at high pressures. The setup includes a custom-made platform and a high-pressure syringe pump. Water bath and heating cartridges will be used to control temperature, and an inverted microscope will be used to observe fluid flow in the chip.

5. REFERENCES

[1] U.S. Energy Information Administration, “World Shale Resource Assessment,” 2015.

[2] U.S. Energy Information Administration, “Annual Energy Outlook 2016,” U.S. Energy Information Administration, 2016.

[3] A. Mehmani, M. Prodanović, and F. Javadpour, “Multiscale, Multiphysics Network Modeling of Shale Matrix Gas Flows,” *Transp. Porous Media*, vol. 99, no. 2, pp. 377–390, Sep. 2013.

[4] R. G. Loucks, R. M. Reed, S. C. Ruppel, and D. M. Jarvie, “Morphology, genesis, and distribution of nanometer-scale pores in siliceous mudstones of the Mississippian Barnett Shale,” *J. Sediment. Res.*, vol. 79, pp. 848–861, 2009.

[5] R. F. Sigal, “Pore-Size Distributions for Organic-Shale-Reservoir Rocks From Nuclear-Magnetic-Resonance Spectra Combined With Adsorption Measurements,” *SPE J.*, vol. 20, 2015.

[6] A. Firoozabadi, *Thermodynamics of Hydrocarbon Reservoirs*. McGraw-Hill Education, 1999.

[7] R. Evans, “Fluids adsorbed in narrow pores: phase equilibria and structure,” *J. Phys. Condens. Matter*, vol. 2, p. 8989, 1990.

[8] M. E. Naraghi and F. Javadpour, “A stochastic permeability model for the shale-gas systems,” *Int. J. Coal Geol.*, vol. 140, pp. 111–124, 2015.

[9] M. Alfi, C. An, Y. Cao, B. Yan, M. A. Barrufet, and J. E. Killough, “Pore Size

Variability and Sieving Effect in Liquid Shale—A Multiple Permeability Approach and Eagle Ford Case Study," in *SPE Reservoir Simulation Conference*, 2017.

[10] M. Alfi, S. A. Hosseini, D. Enriquez, and T. Zhang, "A new technique for permeability calculation of core samples from unconventional gas reservoirs," *Fuel*, vol. 235, pp. 301–305, Jan. 2019.

[11] A. V Neimark and A. Vishnyakov, "Gauge cell method for simulation studies of phase transitions in confined systems," *Phys Rev E Stat Phys Plasmas Fluids Relat Interdiscip Top.*, vol. 62, pp. 4611–4622, 2000.

[12] I. Dukovski, J. Machta, C. Saravanan, and S. M. Auerbach, "Cluster Monte Carlo simulations of phase transitions and critical phenomena in zeolites," *J. Chem. Phys.*, vol. 113, pp. 3697–3703, 2000.

[13] J. Jiang, S. I. Sandler, M. Schenk, and B. Smit, "Adsorption and separation of linear and branched alkanes on carbon nanotube bundles from configurational-bias Monte Carlo simulation," *Phys. Rev. B*, vol. 72, p. 45447, 2005.

[14] E. A. Ustinov and D. D. Do, "Modeling of Adsorption in Finite Cylindrical Pores by Means of Density Functional Theory," *Adsorption*, vol. 11, pp. 455–477, 2005.

[15] Z. Li, Z. Jin, and A. Firoozabadi, "Phase Behavior and Adsorption of Pure Substances and Mixtures and Characterization in Nanopore Structures by Density Functional Theory," *SPE J.*, vol. 19, 2014.

[16] A. W. Islam and A. Y. Sun, "A theory-based simple extension of Peng–Robinson equation of state for nanopore confined fluids," *J. Pet. Explor. Prod. Technol.*, pp.

1–7, 2016.

[17] L. Travalloni, M. Castier, F. W. Tavares, and S. I. Sandler, "Thermodynamic modeling of confined fluids using an extension of the generalized van der Waals theory," *Chem. Eng. Sci.*, vol. 65, pp. 3088–3099, 2010.

[18] L. Travalloni, M. Castier, and F. W. Tavares, "Phase equilibrium of fluids confined in porous media from an extended Peng–Robinson equation of state," *Fluid Phase Equilib.*, vol. 362, pp. 335–341, 2014.

[19] S. P. Tan and M. Piri, "Equation-of-state modeling of confined-fluid phase equilibria in nanopores," *Fluid Phase Equilib.*, vol. 393, pp. 48–63, 2015.

[20] E. G. Derouane, "On the physical state of molecules in microporous solids," *Microporous Mesoporous Mater.*, vol. 104, pp. 46–51, 2007.

[21] T. Pitakbunkate, P. Balbuena, G. J. Moridis, and T. A. Blasingame, "Effect of Confinement on PVT Properties of Hydrocarbons in Shale Reservoirs," *SPE Annual Technical Conference and Exhibition*. Society of Petroleum Engineers, Amsterdam, The Netherlands, 2014.

[22] R. R. Kotdawala, N. Kazantzis, and R. W. Thompson, "Analysis of binary adsorption of polar and nonpolar molecules in narrow slit-pores by mean-field perturbation theory," *J. Chem. Phys.*, vol. 123, p. 244709, 2005.

[23] B. Yan, M. Alfi, Y. Wang, and J. E. Killough, "A New Approach for the Simulation of Fluid Flow In Unconventional Reservoirs Through Multiple Permeability Modeling," *SPE Annual Technical Conference and Exhibition*. Society of Petroleum Engineers, New Orleans, Louisiana, USA, 2013.

[24] M. Alfi, B. Yan, Y. Cao, C. An, J. E. Killough, and M. A. Barrufet, “Microscale porosity models as powerful tools to analyze hydrocarbon production mechanisms in liquid shale,” *J. Nat. Gas Sci. Eng.*, vol. 26, pp. 1495–1505, 2015.

[25] W. J. Stroud, J. E. Curry, and J. H. Cushman, “Capillary Condensation and Snap-off in Nanoscale Contacts,” *Langmuir*, vol. 17, no. 3, pp. 688–698, Feb. 2001.

[26] S. Z. Qiao, S. K. Bhatia, and D. Nicholson, “Study of Hexane Adsorption in Nanoporous MCM-41 Silica,” *Langmuir*, vol. 20, pp. 389–395, 2004.

[27] P. A. Russo, M. M. L. Ribeiro Carrott, and P. J. M. Carrott, “Trends in the condensation/evaporation and adsorption enthalpies of volatile organic compounds on mesoporous silica materials,” *Microporous Mesoporous Mater.*, vol. 151, pp. 223–230, 2012.

[28] R. Radhakrishnan, K. E. Gubbins, A. Watanabe, and K. Kaneko, “Freezing of simple fluids in microporous activated carbon fibers: Comparison of simulation and experiment,” *J. Chem. Phys.*, vol. 111, pp. 9058–9067, 1999.

[29] R. Futamura, S. Ozeki, and T. Iiyama, “An X-ray investigation of the adsorption of methane, water, and their mixtures in carbon micropores,” *Carbon N. Y.*, vol. 85, pp. 8–15, 2015.

[30] S. Liu *et al.*, “Optic Imaging Of Oil/water Flow Behavior In Nano-scale Channels,” *SPE Improved Oil Recovery Symposium*. Society of Petroleum Engineers, Tulsa, Oklahoma, USA, 2014.

[31] M. C. T. Wilson, J. L. Summers, Y. D. Shikhmurzaev, A. Clarke, and T. D. Blake, “Nonlocal hydrodynamic influence on the dynamic contact angle: Slip

models versus experiment," *Phys. Rev. E*, vol. 73, p. 41606, 2006.

[32] M. Hosokawa, M. Naito, T. Yokoyama, and K. Nogi, *Nanoparticle Technology Handbook, 2nd Edition*. Elsevier, 2012.

[33] S. Luo, J. L. Lutkenhaus, and H. Nasrabadi, "Multi-Scale Fluid Phase Behavior Simulation in Shale Reservoirs by a Pore-Size-Dependent Equation of State," *SPE Annual Technical Conference and Exhibition*. Society of Petroleum Engineers, San Antonio, Texas, USA, 2017.

[34] M. Alfi, H. Nasrabadi, and D. Banerjee, "Effect of Confinement on Bubble Point Temperature Shift of Hydrocarbon Mixtures: Experimental Investigation Using Nanofluidic Devices," *SPE Annual Technical Conference and Exhibition*. Society of Petroleum Engineers, San Antonio, Texas, USA, 2017.

[35] M. Alfi, D. Banerjee, and H. Nasrabadi, "Effect of Confinement on the Dynamic Contact Angle of Hydrocarbons," *Energy & Fuels*, vol. 30, no. 11, pp. 8962–8967, Nov. 2016.

[36] T. Funatsu, Y. Harada, M. Tokunaga, K. Saito, and T. Yanagida, "Imaging of single fluorescent molecules and individual ATP turnovers by single myosin molecules in aqueous solution," *Nature*, vol. 374, pp. 555–559, 1995.

[37] L. Wang *et al.*, "Experimental Study and Modeling of the Effect of Nanoconfinement on Hydrocarbon Phase Behavior in Unconventional Reservoirs," in *SPE Western North American and Rocky Mountain Joint Meeting*, 2014.

[38] J. Zhong *et al.*, "Capillary Condensation in 8 nm Deep Channels," *J. Phys. Chem.*

Lett., vol. 9, pp. 497–503, 2018.

[39] L. R. Huang, E. C. Cox, R. H. Austin, and J. C. Sturm, "Continuous Particle Separation Through Deterministic Lateral Displacement," *Science (80-.).*, vol. 304, no. 5673, p. 987 LP-990, May 2004.

[40] P. Abgrall and N. T. Nguyen, "Nanofluidic Devices and Their Applications," *Anal. Chem.*, vol. 80, no. 7, pp. 2326–2341, 2008.

[41] J. Han and H. G. Craighead, "Separation of Long DNA Molecules in a Microfabricated Entropic Trap Array Downloaded from," *Science (80-.).*, vol. 288, 2000.

[42] J. Li, D. Stein, C. McMullan, D. Branton, M. J. Aziz, and J. A. Golovchenko, "Ion-beam sculpting at nanometre length scales," *Nature*, vol. 412, no. 6843, pp. 166–169, Jul. 2001.

[43] M. J. Levene, J. Korlach, S. W. Turner, M. Foquet, H. G. Craighead, and W. W. Webb, "Zero-Mode Waveguides for Single-Molecule Analysis at High Concentrations," *Science (80-.).*, vol. 299, no. 5607, p. 682 LP-686, Jan. 2003.

[44] C. Duan and A. Majumdar, "Anomalous ion transport in 2-nm hydrophilic nanochannels," *Nat. Nanotechnol.*, vol. 5, no. 12, pp. 848–852, Dec. 2010.

[45] Q. Wu, B. Bai, Y. Ma, J. T. Ok, X. Yin, and K. Neeves, "Optic Imaging of Two-Phase-Flow Behavior in 1D Nanoscale Channels," *SPE J.*, vol. 19, pp. 793–802, 2014.

[46] D. Chen and S. Torquato, "Confined disordered strictly jammed binary sphere packings," *Phys. Rev. E*, vol. 92, p. 62207, 2015.

[47] S. Aslan, N. Fathi Najafabadi, and A. Firoozabadi, “Non-monotonicity of the Contact Angle from NaCl and MgCl2 Concentrations in Two Petroleum Fluids on Atomistically Smooth Surfaces,” *Energy & Fuels*, vol. 30, pp. 2858–2864, 2016.

[48] N. S. Kaveh, E. S. J. Rudolph, P. van Hemert, W. R. Rossen, and K. H. Wolf, “Wettability Evaluation of a CO2/Water/Bentheimer Sandstone System: Contact Angle, Dissolution, and Bubble Size,” *Energy & Fuels*, vol. 28, pp. 4002–4020, 2014.

[49] R. W. Smithwich, “Contact-angle studies of microscopic mercury droplets on glass,” *J. Colloid Interface Sci.*, vol. 123, pp. 482–485, 1988.

[50] S. Brandon, N. Haimovich, E. Yeger, and A. Marmur, “Partial wetting of chemically patterned surfaces: The effect of drop size,” *J. Colloid Interface Sci.*, vol. 263, pp. 237–243, 2003.

[51] P. Letellier, A. Mayaffre, and M. Turmine, “Drop size effect on contact angle explained by nonextensive thermodynamics. Young’s equation revisited,” *J. Colloid Interface Sci.*, vol. 314, pp. 604–614, 2007.

[52] H. M. Princen, “Capillary phenomena in assemblies of parallel cylinders,” *J. Colloid Interface Sci.*, vol. 30, pp. 69–75, 1969.

[53] G. Zografi and S. S. Tam, “Wettability of pharmaceutical solids: Estimates of solid surface polarity,” *J. Pharm. Sci.*, vol. 65, pp. 1145–1149, 1976.

[54] W.-C. Liao and J. L. Zatz, “Surfactant solutions as test liquids for measurement of critical surface tension,” *J. Pharm. Sci.*, vol. 68, pp. 486–488, 1979.

[55] A. Marmur, “Equilibrium contact angles: theory and measurement,” *Colloids*

Surfaces A Physicochem. Eng. Asp., vol. 116, pp. 55–61, 1996.

[56] D. Li, “Drop size dependence of contact angles and line tensions of solid-liquid systems,” *Colloids Surfaces A Physicochem. Eng. Asp.*, vol. 116, pp. 1–23, 1996.

[57] D. Li and D. J. Steigmann, “Positive line tension as a requirement of stable equilibrium,” *Colloids Surfaces A Physicochem. Eng. Asp.*, vol. 116, pp. 25–30, 1996.

[58] M.-H. Hong, K. H. Kim, J. Bae, and W. Jhe, “Scanning nanolithography using a material-filled nanopipette,” *Appl. Phys. Lett.*, vol. 77, pp. 2604–2606, 2000.

[59] S. N. Jayasinghe and M. J. Edirisinghe, “Effect of viscosity on the size of relics produced by electrostatic atomization,” *J. Aerosol Sci.*, vol. 33, pp. 1379–1388, 2002.

[60] H. Z. Yu, D. M. Soolaman, A. W. Rowe, and J. T. Banks, “Evaporation of water microdroplets on self-assembled monolayers: from pinning to shrinking,” *Chemphyschem*, vol. 5, pp. 1035–1038, 2004.

[61] D. M. Soolaman and H. Z. Yu, “Water microdroplets on molecularly tailored surfaces: correlation between wetting hysteresis and evaporation mode switching,” *J Phys Chem B*, vol. 109, pp. 17967–17973, 2005.

[62] Y. Zhang, H. R. Lashgari, Y. Di, and K. Sepehrnoori, “Capillary Pressure Effect on Hydrocarbon Phase Behavior in Unconventional Reservoirs,” *SPE Low Perm Symposium*. Society of Petroleum Engineers, Denver, Colorado, USA, 2016.

[63] T. Funatsu, Y. Harada, M. Tokunaga, K. Saito, and T. Yanagida, “Imaging of single fluorescent molecules and individual ATP turnovers by single myosin

molecules in aqueous solution," *Nature*, vol. 374, no. 6522, pp. 555–559, Apr. 1995.

[64] F. Mostowfi, S. Molla, and P. Tabeling, "Determining phase diagrams of gas–liquid systems using a microfluidic PVT," *Lab Chip*, vol. 12, no. 21, p. 4381, Oct. 2012.

[65] Y. Xu, J. Riordon, X. Cheng, B. Bao, and D. Sinton, "The Full Pressure-Temperature Phase Envelope of a Mixture in 1000 Microfluidic Chambers," *Angew. Chemie Int. Ed.*, vol. 56, no. 45, pp. 13962–13967, Nov. 2017.

[66] J. Zhong *et al.*, "Nanoscale Phase Measurement for the Shale Challenge: Multicomponent Fluids in Multiscale Volumes," *Langmuir*, vol. 34, no. 34, pp. 9927–9935, Aug. 2018.

[67] J. Zhong *et al.*, "Condensation in One-Dimensional Dead-End Nanochannels," *ACS Nano*, vol. 11, no. 1, pp. 304–313, Jan. 2017.

[68] M. Alfi, H. Nasrabadi, and D. Banerjee, "Experimental investigation of confinement effect on phase behavior of hexane, heptane and octane using lab-on-a-chip technology," *Fluid Phase Equilib.*, vol. 423, pp. 25–33, 2016.

[69] A.-C. Louër, A. Plecis, A. Pallandre, J.-C. Galas, A. Estevez-Torres, and A.-M. Haghiri-Gosnet, "Pressure-Assisted Selective Preconcentration in a Straight Nanochannel," *Anal. Chem.*, vol. 85, pp. 7948–7956, 2013.

[70] M. Alfi, H. Nasrabadi, and D. Banerjee, "Confinement effects on phase behavior of hydrocarbon in nanochannels," in *ASME 2015 International Mechanical Engineering Congress and Exposition*, 2015.

[71] D.-Y. Peng and D. B. Robinson, “A New Two-Constant Equation of State,” *Ind. Eng. Chem. Fundam.*, vol. 15, pp. 59–64, 1976.

[72] P. M. Sigmund, P. M. Dranchuk, N. R. Morrow, and R. A. Purvis, “Retrograde Condensation in Porous Media,” *SPE J.*, vol. 13, pp. 93–104, 1973.

[73] Y.-O. Shin and J. Simandl, “Vapor and liquid equilibria in porous media,” *Fluid Phase Equilib.*, vol. 166, pp. 79–90, 1999.

[74] A. A. Shapiro and E. H. Stenby, “Thermodynamics of the multicomponent vapor–liquid equilibrium under capillary pressure difference,” *Fluid Phase Equilib.*, vol. 178, pp. 17–32, 2001.

[75] L. Wang, K. Neeves, X. Yin, and E. Ozkan, “Experimental Study and Modeling of the Effect of Pore Size Distribution on Hydrocarbon Phase Behavior in Nanopores,” *SPE Annual Technical Conference and Exhibition*. Society of Petroleum Engineers, Amsterdam, The Netherlands, 2014.

[76] C. F. Weinaug and D. L. Katz, “Surface Tensions of Methane-Propane Mixtures,” *Ind. Eng. Chem.*, vol. 35, pp. 239–246, 1943.

[77] A. S. Danesh, A. Y. Dandekar, A. C. Todd, and R. Sarkar, “A Modified Scaling Law and Parachor Method Approach for Improved Prediction of Interfacial Tension of Gas-Condensate Systems,” *SPE Annual Technical Conference and Exhibition*. Society of Petroleum Engineers, Dallas, Texas, USA, 1991.

[78] A. Danesh, *PVT and phase behaviour of petroleum reservoir fluids*. Elsevier, 1998.

[79] N. Srivastava and M. A. Burns, “Microfluidic pressure sensing using trapped air

compression," *Lab Chip*, vol. 7, pp. 633–637, 2007.

[80] M. Tuller, L. M. Dudley, and D. Or, "Adsorption and capillary condensation in porous media: Liquid retention and interfacial configurations in angular pores," *Subsurf. Hydrol.*, vol. 35, pp. 1949–1964, 1999.

[81] Y. Zeng, *Colloidal Dispersions Under Slit-Pore Confinement*. Springer-Verlag Berlin Heidelberg, 2012.

[82] H. Masuda, H. Yoshida, and K. Higashitani, *Powder Technology: Fundamentals of Particles, Powder Beds, and Particle Generation*. CRC Press, 2006.

[83] R. E. Perry and G. Thodos, "Vapor Pressures of the Light Normal Saturated Hydrocarbons," *Ind. Eng. Chem.*, vol. 44, pp. 1649–1653, 1952.

[84] H. Hendl, E. Bich, and E. Vogel, "A new evaluation of (p, ρ,T) measurements on steam with corrections for the effects of physical and chemical adsorption," *J. Chem. Thermodyn.*, vol. 29, pp. 765–784, 1997.

[85] M. B. Ewing and J. C. S. Ochoa, "The vapour pressures of n-octane determined using comparative ebulliometry," *Fluid Phase Equilib.*, vol. 210, pp. 277–285, 2003.

[86] J. D. Bernardin, I. Mudawar, C. B. Walsh, and E. I. Franses, "Contact angle temperature dependence for water droplets on practical aluminum surfaces," *Int. J. Heat Mass Transf.*, vol. 40, pp. 1017–1033, 1997.

[87] F. D. Petke and B. R. Ray, "Temperature dependence of contact angles of liquids on polymeric solids," *J. Colloid Interface Sci.*, vol. 31, pp. 216–227, 1969.

[88] R. Deshpande, D. M. Smith, and C. J. Brinker, "Preparation of high porosity

xerogels by chemical surface modification." Google Patents, 1996.

[89] B. T. Ingram, "Wetting of silica by n-alkanes," *J. Chem. Soc. Faraday Trans. 1 Phys. Chem. Condens. Phases*, vol. 70, pp. 868–876, 1974.

APPENDIX: MATLAB CODES FOR MODELING PART

MATLAB Codes for Calculation of bubble point temperature using the capillary pressure model.

```
% Solve the bubble point of confined fluids
% apply PR-EOS
% apply surface tension models

% System C8
% Pc, Tc obtained from Thermodynamics of Hydrocarbon Reservoirs
% w obtained from B. E. Poling, J. M. Prausnitz, J. P. O’Connell, The Properties of Gases and Liquids, McGraw-Hill, New York, 2001.
% Parachors obtained from PVT and Phase Behaviour of Petroleum Reservoir Fluids (Ali Danesh 1998)


clear all
clc


% Input
PL = 1.013*10^5; % liquid pressure [Pa]
Tb0 = [398.82]; %component bubble points at given pressure (1.013*10^5 Pa) [K]
Psat = [4118.9983]; %components vapor pressure at 313.15 K [Pa]
sigmaPC = [0.02162]; %surface tension of pure components against air[N/m] at room temperature
```

```
% unknown T = temperature [K]
Pc = [2.495*10^6]; %component 1,2 [Pa]
Tc = [568.7]; %component 1,2 [K]
x = [1]; %component 1,2, liquid phase
MW = [114.23]; %component 1,2 molecular weight [kg/mol]
w = [0.3765]; %acentric factor, component 1,2
delta = [0];% binary interaction coefficients delta (component 1,2) for PR-EOS

Pcr = [351.5]; %Parachors, component 1,2
theta = 75/180*3.1415926; %contact angle [rad]


% Inside variables
% T0 = initial guess of mixture bubble point
% Pc = PV - PL = 4*sigma*cos(theta)/d [Pa]
% Pc0, Pc1 capillary pressure [Pa]
% k iteration count
% ZL = liquid phase compressibility
% fL = liquid phase fugacity
% atotal = a in PREOS
% aa(i,j)
% AL = A in PREOS
% BL = B in PREOS
% Similarly, ZV, fV, atotalV, aaV, btotalV, bV, AV, BV = vapor phase properties
% i, j, k number count
% dy = dy in approximate dFdy
% dY = iteration addition obtained by solving Jacobian equation
```

```
nc = length(x); %count the number of components
% Naming liquid phase as phase 1, vapor phase as phase 2
Ph(1) = 'L';
Ph(2) = 'V';

% initial guess of bubble point
T0 = sum(Tb0.*x);

aaa=5*10^-6;
bbb=100*10^-9;
d = 2*aaa*bbb/(aaa+bbb); %confining pore diameter [m]

% initial guess of surface tension
sigma0 = sum(sigmaPC.*x);
Pc0 = 4*sigma0*cos(theta)/d;
PV = PL + Pc0;
%y0 = x.*Psat./sum(x.*Psat) %not accurate because Psat(1) and Psat(2) are significantly different

% 1. Estimate (Tb, y1) search composition for y and increasing temperature for T
for k = 1:nc
   K(k)=Pc(k)/PL*exp(5.37*(1+w(k))*(1-Tc(k)/T0));
   y(k)=K(k)*x(k);
end
ymin = y./sum(y);

fV = 10000000000000;
fL = 10;
```

```
k = 0;
T = T0;
while sum(abs((log(fV./fL).*x))) > 0.01 && k < 100
   k = k + 1;
   T = T + 5;
   [ ZV, fV, phiV, atotalV, aaV, btotalV, bV, AV, BV ] = PR( PV, T, Pc, Tc, ymin, w, delta, Ph(2));
   [ ZL, fL, phiL, atotalL, aaL, btotalL, bL, AL, BL ] = PR( PL, T, Pc, Tc, x, w, delta, Ph(1));
   R2(k) = (1/T)*sum(abs((log(fV./fL).*x)));

end
[R2min, I2] = min(R2);
T = T0+I2*5;


%phiV
%phiL
%k
%T



% 2. Newton-Raphson methods obtaining the roots

F = 1;
s = 0;
while sum(abs(F)) > 10^-5 && s < 20000
   s = s + 1; %iteration step count
```

```
                if s >= 20000
                disp('iteration exceeds the limit for diameter')
                d
                end



                % Update interfical tension model
                sigma = IFT( x, y, PL, PV, T, ZL, ZV, Pcr );
                %sigma = 0.001;
                Pc1 = 4*sigma*cos(theta)/d;
                PV = PL+Pc1;



               [ ZV, fV, phiV, atotalV, aaV, btotalV, bV, AV, BV ] = PR( PV, T, Pc, Tc, y, w,
delta, Ph(2));
               [ ZL, fL, phiL, atotalL, aaL, btotalL, bL, AL, BL ] = PR( PL, T, Pc, Tc, x, w,
delta, Ph(1));
            for i = 1:nc
                F(i) = y(i) - x(i)*phiL(i)/phiV(i)*PL/PV;
                F(nc+1) = 1 - sum(y);
            end

            % Calculate dFdy(i,j) dFdT
            dy = 0.00000001;
            dT = 0.000001;
            for i = 1:nc
                for j = 1:nc
                    y(j) = y(j) + dy;
```

```
            [ ZV, fV, phiV, atotalV, aaV, btotalV, bV, AV, BV ] = PR( PV, T, Pc, Tc,
y, w, delta, Ph(2));
            [ ZL, fL, phiL, atotalL, aaL, btotalL, bL, AL, BL ] = PR( PL, T, Pc, Tc, x,
w, delta, Ph(1));
            Fplus(i,j) = y(i) - x(i)*phiL(i)/phiV(i)*PL/PV;
            dFdy(i,j) = (Fplus(i,j) - F(i))/dy;
            y(j) = y(j) - dy;
         end

         T = T + dT;
         [ ZV, fV, phiV, atotalV, aaV, btotalV, bV, AV, BV ] = PR( PV, T, Pc, Tc, y,
w, delta, Ph(2));
         [ ZL, fL, phiL, atotalL, aaL, btotalL, bL, AL, BL ] = PR( PL, T, Pc, Tc, x, w,
delta, Ph(1));
         Fplus(i,nc+1) = y(i) - x(i)*phiL(i)/phiV(i)*PL/PV;
         dFdT(i,nc+1) = (Fplus(i,nc+1) - F(i))/dT;
         T = T - dT;  %change T to orginal value in the loop at the end of the loop
      end

      for i = 1:nc
         for j = 1:nc
            J(i,j) = dFdy(i,j);
         end
         J(i,nc+1) = dFdT(i,nc+1);
      end
      for j = 1:nc
         J(nc+1,j) = -1;
      end
```

```
J(nc+1, nc+1) = 0;
J;

R = -F;
dY = R/J;

% Update vector y, T
for i = 1:nc
   yy(i) = y(i) + dY(i); %updated composition yy(i)
end

for i = 1:nc
   y(i) = yy(i)/sum(yy);
end

T = T + dY(nc+1);
y;

end
```

Calculating interfacial surface tension:

```
function [ sigma ] = IFT( x, y, PL, PV, T, ZL, ZV, Pcr )
% Interfacial tension model: Danesh, A.S., Dandekar, A.Y., Todd, A.C.,and SarkarR., A Modified Scaling Law and Parachor Method Approach for Improved Prediction of Interfacial Tension of Gas-Condensate Systems
% Input
```

```
    % x = liquid composition, x(1)+x(2)+...+x(c)=1
    % y = vapor composition, y(1)+y(2)+...+y(c)=1
    % PL = liquid phase pressure [Pa]
    % PV = vapor phase pressure [Pa]
    % T = temperature [K]
    % ZL, ZV = liquid, vapor phase compressibilities
    % Pcr = Parachor of components 1,...,c

    % Inside constants
    % R = gas law constants 8.314 [m3 Pa/(gmol K) = J/gmol-K]

    % Inside Variables
    % c = components number
    % sigmaE = sigma^(1/E)
    % E
    % i, j, k, s = #count

    % Declare constants
    R = 8.314; %[m3 Pa/(gmol K) = J/gmol-K]

    nc = length(x);
    sigmaE = 0;
    for i = 1:nc
       sigmaE = sigmaE + Pcr(i)*(x(i)*PL/(ZL*R*T) -
y(i)*PV/(ZV*R*T))/(1000^2);

    end
    E = 3.583 + 0.16*(PL/(1000^2*ZL*R*T)-PV/(1000^2*ZV*R*T));
    sigma = ((abs(sigmaE))^E)/1000; %/1000 mN/m to N/m
```

```
        end
```

Main Function:

```
function [ Z, f, phi, atotal, aa, btotal, b, A, B ] = PR( P, T, Pc, Tc, x, w, delta, Ph)
% Peng-Robinson EOS calculation of Z

% Input
% P = pressure [Pa]
% T = temperature [K]
% Pc = critical pressure (components 1,...,c) [Pa]
% Tc = critical temperature (components 1,...,c) [K]
% x = composition, x(1)+x(2)+...+x(c)=1
% w = acentric factor (components 1,...,c)
% delta = interaction parameter (components 1,...,c)
% Ph = phase L/V

% Inside Constants
% R = gas law constants 8.314 [m3 Pa/(gmol K) = J/gmol-K]

% Inside Variables
% nc = number of components
% a = 0.45724*R^2*Tc^2/Pc^2
% b = 0.07780*R*Tc/Pc
% A = atotal*P/(R^2*T^2)
% B = btotal*P/(R*T)
```

```
% Tr = Reduced pressure (components 1,...,c)
% m (components 1,...,c)
% i, j, k, s = #count
% aa(i,j)
% atotal
% btotal
% C = coefficients of a polynomial
% phi = fugacity coefficient (components 1,...,c)
% f = fugacity
% phi = fugacity coefficient

% Declare constants
R = 8.314;

nc = length(x);
Tr = T./Tc;
for i = 1:nc
if w(i) > 0 && w(i) <= 0.1
   m(i) = 0.37464 + 1.54226*w(i) - 0.26992*w(i)^2;
elseif w(i) > 0.1 && w(i) < 2.0
      m(i) = 0.3796 + 1.485*w(i) - 0.1644*w(i)^2 + 0.01667*w(i)^3;
else
   disp('w(i) wrong')
end
alpha(i) = (1 + m(i)*(1-Tr(i)^0.5))^2;
end

% calculate atotal, btotal
a = 0.45724*R^2.*Tc.^2./Pc.*alpha;
```

```
b = 0.07780*R.*Tc./Pc;
atotal = 0;
btotal = 0;
for i = 1:nc

    for j = 1:nc
        aa(i,j) = (1 - delta(i,j))*a(i)^0.5*a(j)^0.5;
        atotal = atotal + x(i)*x(j)*aa(i,j);
    end
end
for i = 1:nc
    btotal = btotal +b(i)*x(i);
end

% Calculate the roots of PR-function(Z)
A = atotal*P/(R^2*T^2);
B = btotal*P/(R*T);
C(1) = 1;
C(2) = -(1-B);
C(3) = A-3*B^2-2*B;
C(4) = -(A*B-B^2-B^3);
Z0 = roots(C);
Z0 = Z0(Z0 == real(Z0));


if Ph == 'L'
    Z = min(Z0(Z0>B)); %Z0(Z0>0) select positive Z0 elements
else
    Z = max(Z0(Z0>B));
```

```
end

for i = 1:nc
    phi(i) = exp(b(i)/btotal*(Z - 1) - log(Z - B) - A/(2*2^0.5*B)*(2*sum(x.*aa(i,:))/atotal
- b(i)/btotal)*... %(x*(aa(i,:)')problem
    log((Z + 2.414*B)/(Z - 0.414*B)));
    f(i) = x(i)*phi(i)*P;
end

end
```